



# Euler-Lagrange numerical simulation of improved magnetic drug delivery in a three-dimensional CT-based carotid artery bifurcation



Hiwa Aryan <sup>a,b</sup>, Borhan Beigzadeh <sup>a</sup>, Majid Siavashi <sup>b,\*</sup>

<sup>a</sup> Biomechatronics and Cognitive Engineering Research Laboratory, School of Mechanical Engineering, Iran University of Science and Technology, Tehran, Iran

<sup>b</sup> Applied Multi-Phase Fluid Dynamics Laboratory, School of Mechanical Engineering, Iran University of Science and Technology, Tehran, Iran

## ARTICLE INFO

### Article history:

Received 20 December 2021

Revised 11 March 2022

Accepted 24 March 2022

### Keywords:

Magnetic drug delivery (MDD)

Carotid bifurcation

Superparamagnetic iron oxide nanoparticles (SPIONs)

Non-Newtonian

Euler-Lagrange two-phase flow

Finite element method (FEM)

## ABSTRACT

**Background and objective:** Magnetic drug targeting (MDT) is a promising method to improve the therapy efficiency for cardiovascular diseases (CVDs) and cancers. In MDT, therapeutic agents are bonded to superparamagnetic iron oxide nanoparticle (SPION) cores and then are guided toward the damaged tissue through a magnetic field. Fundamentally, it's vital to steer the SPIONs to the desired location to increase the capture efficiency at the target lesion. Hence, the present study aims to enhance the drug delivery to the desired branch in a carotid bifurcation. Besides, it is tried to decrement the particles' entry to the unwanted outlet by using four different magnet configurations (with a maximum magnetic flux density of 0.4 T) implanted adjacent to the artery wall. Also, the effect of particles' diameter -ranging from 200 nm to 2  $\mu\text{m}$ - on the drug delivery performance is studied in the four cases.

**Methods:** The Eulerian-Lagrangian approach with one-way coupling is employed for numerical simulation of the problem using the finite element method (FEM). The dominant forces acting on particles are drag and magnetophoretic. A computed tomography (CT) model of the carotid bifurcation is adopted to have a 3D realistic geometry. The blood flow is considered to be laminar, incompressible, pulsatile, and non-Newtonian. Boundary conditions are applied using the three-element Windkessel equation.

**Results:** Results are presented in terms of velocity, pressure, magnetic field flux density, wall shear stress, and streamlines. Also, the number of particles in each direction is presented for the four studied cases. The results show that using proper magnets configurations makes it possible to guide more particles to the desired branch (up to 4%) while preventing particles from entering the unwanted branch (up to 13%). By defining connectivity between oscillatory shear index (OSI) value and magnetic drug delivery efficacy, it becomes clear that places with lower OSI values are more proper to place the magnets than areas with higher OSI values.

**Conclusions:** It was observed that increasing the diameter of particles does not necessarily result in a higher drug delivery efficiency. The configuration of the magnets and the size of particles are the main affecting parameters that should be chosen precisely to meet the most efficient drug delivery performance.

Magnetic drug targeting (MDT) is a promising method to improve the therapy efficiency for cardiovascular diseases (CVDs) and cancers. Fundamentally, it's vital to steer the superparamagnetic iron oxide nanoparticles (SPIONs) to the target lesion location to increase the capture efficiency. Hence, the present study aims to enhance the drug delivery to the desired branch in a 3D carotid bifurcation. Besides, it is tried to decrement the particles' entry to the unwanted outlet by using four different magnet configurations implanted adjacent to the artery wall.

The Eulerian-Lagrangian approach with one-way coupling is employed for numerical simulation of the problem using the finite element method (FEM). The dominant forces acting on particles are drag and magnetophoretic. The blood flow is laminar, incompressible, pulsatile, and non-Newtonian.

The results show that it is possible to guide more particles to the desired branch (up to 4%) while preventing particles from entering the unwanted branch (up to 13%). By defining connectivity between oscillatory shear index (OSI) value and magnetic drug delivery efficacy, it becomes clear that places with lower OSI values are more proper to place the magnets than areas with higher OSI values.

© 2022 Elsevier B.V. All rights reserved.

\* Corresponding author at: School of Mechanical Engineering, Iran University of Science and Technology, Iran

E-mail addresses: [hiwa\\_aryan@mecheng.iust.ac.ir](mailto:hiwa_aryan@mecheng.iust.ac.ir) (H. Aryan), [b\\_beigzadeh@iust.ac.ir](mailto:b_beigzadeh@iust.ac.ir) (B. Beigzadeh), [m.siaavashi@iust.ac.ir](mailto:m.siaavashi@iust.ac.ir) (M. Siavashi).

## Nomenclature

### Symbols

$\mathbf{B}$ [T]	applied magnetic field
$C$ [ $\text{m}^3/\text{Pa}$ ]	capacitance
$C_D$ [-]	drag coefficient
$d_p$ [m]	Particle diameter
$\mathbf{F}_D$ [N/kg]	Drag force per unit mass of the particle
$\mathbf{F}_M$ [N/kg]	magnetophoretic force per unit mass of the particle
$\text{Fr}$ [-]	particle Froude number
$\mathbf{H}$ [H/m]	induced magnetic field
$K$ [-]	Clausius-Mossotti factor
$M$ [A/m]	Magnetization
$m_p$ [kg]	Particle mass
$\mathbf{n}$ [-]	the normal unit vector of the tangential plane to the vessel wall
$n$ [-]	power index
$p$ [Pa]	Fluid pressure
$P_{\text{Pe}}$ [-]	particle Peclet number
$P_{\text{out}}$ [Pa]	outlet pressure
$Q_{in}$ [ $\text{m}^3/\text{s}$ ]	Inlet flow rate
$r$ [m]	particles radius
$R_d$ [Pa, s/ $\text{m}^3$ ]	Distal resistance
$R_p$ [Pa, s/ $\text{m}^3$ ]	Proximal resistance
$Re$ [-]	Reynolds number
$Re_G$ [-]	shear Reynolds number
$Re_p$ [-]	particle Reynolds number
$\mathbf{u}$ [m/s]	Fluid velocity vector
$\mathbf{u}_p$ [m/s]	particle velocity vector
$\mathbf{v}$ [m/s]	Particle velocity vector

### Greek symbols

$\varepsilon$ [-]	dimensionless particle diameter
$\dot{\gamma}$ [1/s]	strain rate
$\lambda$ [s]	relaxation time
$\mu$ [Pa, s]	Dynamic viscosity
$\mu_0$ [H/m]	magnetic permeability of vacuum
$\mu_0$ [Pa, s]	zero-shear rate viscosity
$\mu_r$ [H/m]	the relative magnetic permeability of the surroundings
$\mu_{rb}$ [H/m]	the magnetic permeability of blood
$\mu_{rp}$ [H/m]	particle magnetic permeability
$\mu_\infty$ [Pa, s]	infinite shear rate viscosity
$\rho$ [kg/m <sup>3</sup> ]	density of fluid
$\rho_f$ [kg/m <sup>3</sup> ]	density of blood
$\rho_p$ [kg/m <sup>3</sup> ]	density of particle
$\tau_{mag}$ [Pa]	time mean magnitude of the wall shear stress
$\tau_{wall}$ [Pa]	Instantaneous Wall shear stress
$\chi$ [-]	Fluid to particle density ratio
$\chi_p$ [-]	magnetic susceptibility of the particle

### Acronyms

BPM	beats per minute
CCA	common carotid artery
CE	capture efficiency
CT	computed tomography
CVDs	Cardiovascular diseases
DDEI	drug delivery efficiency increment
ECA	external carotid artery
FEM	finite element method
ICA	internal carotid artery
MCNPs	multi-core nanoparticles
MDD	magnetic drug delivery

MDT	magnetic drug targeting
MNPs	magnetic nanoparticles
MRI	magnetic resonance imaging
ODE	ordinary differential equation
OSI	oscillatory shear index
PDEs	Partial differential equations
PEG	Polyethylene glycol
PVA	Polyvinyl alcohol
RBC	red blood cell
RCR	Resistance, capacitor, and resistance
SPIONs	Superparamagnetic iron oxide nanoparticles
TAWSS	Time average wall shear stress magnitude
TDD	targeted drug delivery
WSS	wall shear stress

## 1. Introduction

Cardiovascular diseases (CVDs) and cancer are the first and the second leading causes of death worldwide, respectively [1,2]. So, their diagnosis and treatment methods need to be improved continuously. Nowadays, some conventional techniques such as systemic administration, radiotherapy, chemotherapy, and surgery [3–5] are employed to cure these illnesses. These treatments are invasive [3] have a toxicity nature [4] with the risk of mortality during surgery [5]. Also, they have significant side effects [6] (such as neurotoxicity, hair loss, nausea [7], bone marrow ailments [8], infection, mucositis, diarrhea [9], nephro- and cardio-toxicity, intestinal injury, and anemia), as well as minor symptoms (like uneasiness, nausea and, fatigue) [10]. Over the last few decades, researchers have placed an interest in developing new non-invasive therapeutic methods to maximize efficiency and minimize the adverse side effects of conventional treatment procedures. To achieve this target, concentrating the drug in the desired location can prevent the entire body from being affected by the drug. Hence, a higher concentration in the target tissue with subsequent fewer side effects can be obtained with less medicine [11,12].

Among novel physical, chemical, and biological targeted drug delivery (TDD) methods [11], the magnetic drug delivery (MDD), also known as magnetic drug targeting (MDT), is a promising, minimally invasive, and efficient physical method to steer the pharmaceutical agents at the desired location [13]. The principle of MDT is to bond the drug to a magnetic core and drive it to the target tissue in the patient's body by a magnetic field [13]. The magnetic core as the drug carrier in MDT should have some unique physicochemical characteristics. These characteristics include the size, shape, core fabrication methods, magnetic properties, surface quality, drug loading, and coating properties [1,14,16]. Drug carriers in MDT should be small enough in order of a red blood cell (RBC) around  $6\mu\text{m}$  [17]-to circulate through the circulatory system without causing blockage. So magnetic nanoparticles (MNPs) are in great interest for MDT [18] with lots of therapeutic and diagnosis applications in medicine like drug delivery, hyperthermia, anemia chronic kidney disease, disorders associated with the musculoskeletal system and MRI [19]. The other vital property for therapeutic MNPs is superparamagnetism. Unlike ferromagnetism materials, superparamagnetic particles have no remanent magnetization after removing the magnetic field, preventing the MNPs from causing embolus [15,17]. To improve the effectiveness of MDT, materials with high saturated magnetization such as transition metals (e.g., Fe, Co, Ni) and metal oxides (e.g.,  $\text{Fe}_3\text{O}_4$ (Magnetite),  $\gamma - \text{Fe}_2\text{O}_3$  (Maghemite)) are in great interest [20,21]. Particularly iron oxides have low toxicity, and the human body can store and use them for biological mechanisms [14,22,23]. Superparamagnetic iron oxide nanoparticles (SPIONs) are used as

the magnetic core in MDT. For optimizing the bio-compatibility and bio-deterioration of SPIONs, some natural or synthetic polymer matrices (e.g., dextran, chitosan, PEG, and PVA) are used as coating of the SPIONs [19,24]. By increasing the core size, superparamagnetism changes into ferromagnetism. So another novel method to overcome this problem for the synthesis of larger carriers is producing multi-core nanoparticles (MCNPs) which contain multi superparamagnetic iron oxide cores in one matrix [17,22]. Manipulating the combination of the magnetic core, therapeutic agent, and the biocompatible coating to the target tissue is achieved by an external or internal magnetic field. Such magnetic fields can be generated by an outside placed or inside (or implanted) single permanent magnet, an array of permanent magnets, static field electromagnets, and varying field magnet systems [25,26]. Furthermore, it's necessary to know that MDT is not possible just by a uniform magnetic field, no matter how strong. Hence, a sufficient magnetic field gradient is needed to perform an efficient MDT [14]. To maintain safety, researchers have proposed some limits of exposure to magnetic fields for the human body in therapeutic and diagnosis clinical trials [27].

From the 1970s, when Freeman et al. [28] introduced the first concept of using magnetic materials in medicine, many experimental and numerical research studies have been done in the MDT field. This idea has led to the promising novel medical applications of MNPs, in the last two decades [29,30]. In general, MDT researches are in three main areas: 1- in body airways that transfer the air from nasal cavity and mouth to the alveolus [31–33]; 2- from blood capillaries to interstitial fluids [34,35]; and in 3- blood arteries that are relevant to this article scope. Two-phase flow simulation models can be used to simulate MDT problems. The Euler-Euler and Euler-Lagrange methods are the two main simulation techniques of MDT. In the Euler-Euler approach, both phases are assumed to be continuous, while in the Euler-Lagrange approach, the base fluid is treated as the continuum phase, and the MNPs are considered as the discrete phase [36,37]. Among these techniques, the Euler-Lagrange model is capable of showing the trajectories of MNPs [38]. The particle size, particle's magnetic properties, magnetic field flux density and its gradient, boundary conditions, and the particle releasing method are the most influencing studied parameters.

By considering the Euler-Lagrange approach and two different magnetic sources, Wang et al. [39] numerically investigated a MDT problem. They modeled the vessel as a cylinder and explored the efficiency of capturing MNPs in the desired location with different magnetic flux densities, particle diameters, and inlet flow velocities. Their results showed that increasing the particle's diameter and the magnetic flux density increases the capture efficiency (CE). In contrast, the opposite fact was observed by the increase in the inlet flow velocity. Larimi et al. [37] numerically investigated the effect of the size of MNPs on their trajectories in a 2D symmetrical bifurcation in the presence of a magnetic field using the Euler-Lagrange method. They showed that the larger the particle is, the more particles are attracted through the position of the wire. Bose and Banerjee [40] studied the effect of various magnetic field flux densities, as high as 25 T, and inlet constant flow velocities on the CE of MNPs in a 2D stenosed bifurcation. They showed that by increasing the size of the particles and the strength of the magnetic field, the CE increases. Their work also illustrated that CE decreases by increasing the base flow Reynolds number (Re). Lunnoo and Puangmali [41] considered the effectiveness of using a magnet with a maximum field strength of 2 T in a mimicked 2D arterial flow with a pulsatile inlet velocity and constant outlet pressure boundary conditions. They used different iron-oxide particles with various sizes as the core in MDT to analyze the CE. Their results indicate that  $Fe_3O_4$  particles have the best CE among other studied magnetic cores. Also, they observed that the coating

of MNPs has no noticeable effect on the trajectory of the particles. Larimi et al. [42] used a 2 T magnetic field and a two-way coupling method to investigate the effect of non-Newtonian blood flow characteristics and particle size on MDT in a 3D symmetrical bifurcation vessel. Their results revealed that by using larger particles the average volume fraction of MNPs in the target region increased. Hoshiar et al. [43] in experimental and numerical studies demonstrated the effectiveness of MDT in a Y-shaped 2D channel to steer the particles with different sizes and different inlet flow velocities to the desired branch outlet. They showed that by using a magnetic field, the number of particles reaching to the target outlet increases. Manshadi et al. [44] used a 2D four-layer channel geometry and constant inlet blood velocity to evaluate the CE of MNPs in the desired location considering different particles sizes and magnetic properties. They showed that larger MNPs are more likely to be captured by the magnetic field at the region of interest, and a stronger magnetic field increases the number of trapped particles. They also showed that releasing the particles closer to the magnetic field source increases the CE. Hewlin et al. [2] evaluated the CE of magnetite core particles in a healthy and a stenosis realistic carotid bifurcation model with pulsatile inlet flow velocity and Windkessel outlet boundary condition. Their results showed that the larger particles have a better CE, and by increasing the magnetic field flux density, the CE of the particles increases too. Hoshiar et al. [13] used a 2D multi-bifurcation network to perform MDT and steer the particles to the desired outlet. They compared the numerical results with experimental data, revealing that a small inlet velocity with a strong magnetic field could make MDTs more efficient. Sodagar et al. [45] numerically investigated MDT in a synthetic 3D model of the aortic artery with the Eulerian-Lagrangian approach by applying the non-Newtonian viscosity and oscillating input blood flow. The effect of particles' diameter and the position of the wire on CE are investigated. The results showed that larger particles have higher absorption efficiency. The number of particles that enter the different parts of the aortic arch is affected by the direction of the magnetic field. Using two different magnet array configurations, Lindemann et al. [46] evaluated MDT's effectiveness in a 3D geometry of a microvascular network. Parameters like magnetic field gradient and particles diameter were investigated, and the outcome shows that closer magnets could provide a higher CE.

The above literature review shows that many works in the MDT field have not used the anatomical arteries model and physiological boundary conditions. Since 2D geometries and 3D symmetrical ones are not proper models for the simulation of a realistic vessel, they cannot reflect the geometric complexities of a natural artery. Also, the flow pulsation effect is an effective tool in many configurations for controlling the fluid flow features [47]. So the constant inlet blood velocity and outlet pressure do not apply the physiological boundary conditions at the inlet and outlet of the artery. Most of the previous studies have focused on the targeting concept of MDT. At the same time, it's also essential to guide the therapeutic agents to the desired location before absorption, especially in a bifurcation. Additionally, using magnetic fields has some limitations in generation and employment, which have not been appropriately considered in most previous works. For example, the maximum remanence of a single permanent magnet can reach about only 1.5 T [26], and exposure to magnetic fields is limited [48].

This study firstly aims to simulate pulsatile, non-Newtonian blood flow in a 3D realistic carotid artery bifurcation model using a three-element Windkessel (RCR) boundary condition at the outlets. Secondly, by employing the Euler-Lagrange method, different permanent magnet arrangements are considered to find the MDT efficiency according to the target outlet and the undesired one. Furthermore, the effect of flow parameters and magnets placement on MDT efficiency is investigated. An appropriate magnet arrangement

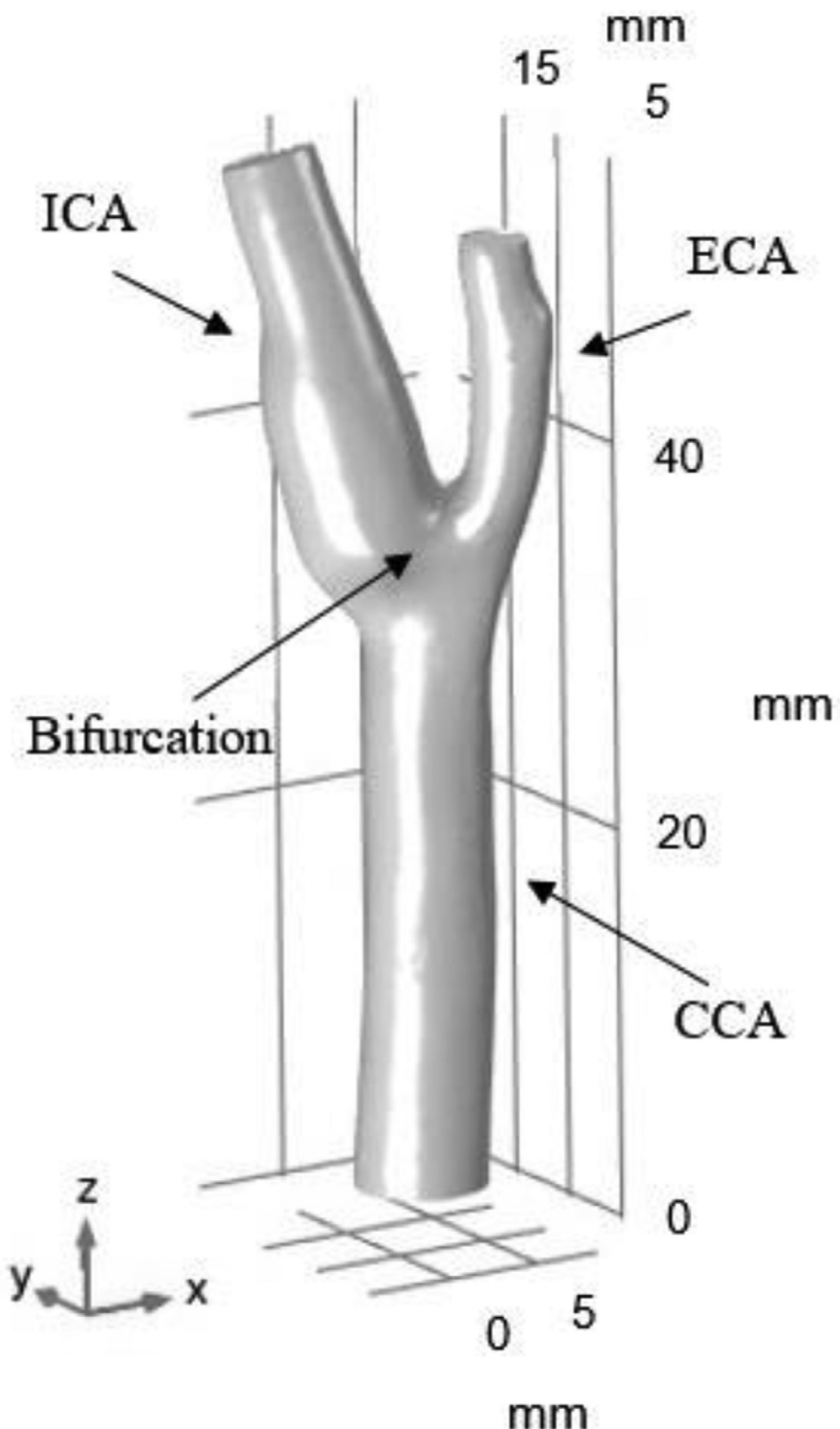


**Fig. 1.** The 3D geometry of the carotid artery used in this work.

is proposed to conduct the MNPs toward the desired branch of the carotid bifurcation.

## 2. Materials and methods

### 2.1. Geometry

The model geometry used in this work is a 3D carotid artery bifurcation [49], consisting of a common carotid artery (CCA), inter-

nal carotid artery (ICA), and external carotid artery (ECA) branches (see Fig. 1). Some more details about the following geometry are presented in Table 1.

### 2.2. Boundary conditions

#### 2.2.1. Fluid phase

According to previous research, MDT and MDD can be more efficient when the base fluid has a lower velocity (or lower Re num-

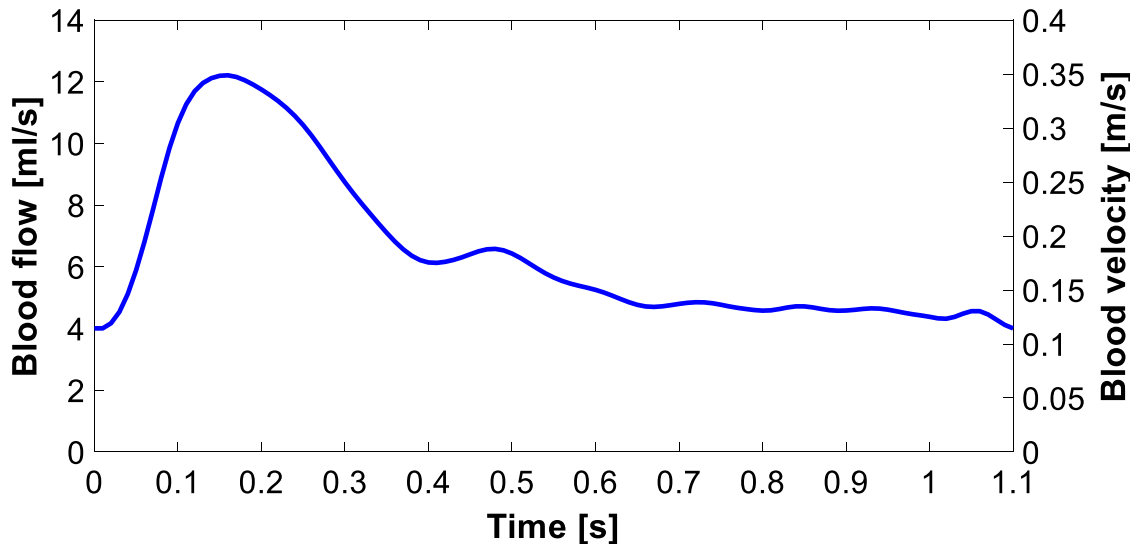


Fig. 2. CCA inlet boundary condition [50].

**Table 1**

Details of the model geometry and its boundaries.

Boundary:	CCA inlet	ICA outlet	ECA outlet	Wall
Area [mm <sup>2</sup> ]	34.71	17.49	9.12	1353

**Table 2**

Inlet flow series of equations.

Flow equations [ml/s]	Time [s]
$-48840t^4 + 2898t^3 + 1030t^2 - 14.75t + 4$	$0 \leq t \leq 0.1202$
$90620t^4 - 57610t^3 + 13390t^2 - 1347t + 61.53$	$0.1202 \leq t \leq 0.2060$
$-7385t^4 + 9606t^3 - 4569t^2 + 909t - 52.26$	$0.2060 \leq t \leq 0.3850$
$79300t^4 - 135200t^3 + 86550t^2 - 24650t + 2640.87$	$0.3850 \leq t \leq 0.4520$
$23650t^4 - 45250t^3 + 32200t^2 - 10100t + 1184.56$	$0.4520 \leq t \leq 0.5566$
$21060t^4 - 50720t^3 + 45720t^2 - 18290t + 2746.2$	$0.5566 \leq t \leq 0.6542$
$-2089t^3 + 4347t^2 - 3011t + 699$	$0.6542 \leq t \leq 0.7178$
$2174t^3 - 4918t^2 + 3703t - 923.26$	$0.7178 \leq t \leq 0.8001$
$-3708t^3 + 9144t^2 - 7511t + 2059.7$	$0.8001 \leq t \leq 0.8568$
$-897.4t^3 + 2499t^2 - 2316t + 719$	$0.8568 \leq t \leq 0.9512$
$221.4t^3 - 602.2t^2 + 538.2t - 153$	$0.9512 \leq t \leq 1.0103$
$-13050t^3 + 40560t^2 - 42010t + 14504.66$	$1.0103 \leq t \leq 1.0531$
$8653t^3 - 28040t^2 + 30270t - 10881.743$	$1.0531 \leq t \leq 1.1000$

ber), making the flow laminar. Usually, higher heartbeat rates result in higher blood velocity in the arteries. Accordingly, the heartbeat rate can be reduced by using drugs for drug delivery purposes. Hence, a pulsatile blood flow with approximately 55 beats per minute (BPM) is chosen as the fully developed flow. The CCA inlet boundary condition is adapted from the work of Boileau et al. [50] (as exhibited in Fig. 2) and is presented through the polynomials summarized in Table 2.

The three-element Windkessel boundary condition (RCR) is applied at the ICA and ECA outlets. RCR boundary condition is an ordinary differential equation (ODE) that relates the inlet flow rate and its time derivative to the outlet pressure and its time derivative. As shown in Fig. 3, this boundary condition is illustrated as a circuit with two resistances ( $R_p$  and  $R_d$ ) and a capacitor ( $C$ ) [2], showing the friction due to viscous dissipation and the compliance of the vessel wall, respectively [51].

The RCR parameters used in this work are presented in Table 3 [50]. The following equation describes the RCR differential equation [50].

$$Q \left( 1 + \frac{R_p}{R_d} \right) + CR_p \frac{\partial Q}{\partial t} = \frac{P_{out}}{R_d} + C \frac{\partial P_{out}}{\partial t} \quad (1)$$

**Table 3**

The Windkessel boundary condition (RCR) parameters used in Eq. (1) [50].

Parameter	ICA	ECA
$R_p$ [Pa.s/m <sup>3</sup> ]	$5.760 \times 10^8$	$9.391 \times 10^8$
$R_d$ [Pa.s/m <sup>3</sup> ]	$2.3041 \times 10^9$	$3.7563 \times 10^9$
$C$ [m <sup>3</sup> /Pa]	$9.833 \times 10^{-11}$	$6.032 \times 10^{-11}$

The artery wall is assumed to be rigid with no fluid source or sink, and the non-slip boundary condition is applied to it [52,53]. The final output diagrams for ICA and ECA outlet pressure boundary conditions in one cycle are shown in Fig. 4. Comparing the CCA boundary with ICA and ECA boundaries reveals a time delay between the peak of the velocity profile and the maximum value of the pressure profile due to the compliance of the downstream vasculature, mentioned as a capacitance in the RCR boundary condition.

### 2.2.2. Particle phase

Totally 11000 MNPs with diameters in the range of (200-2000) [nm] in each release continuously enter through the inlet boundary during one cycle. The initial velocity of MNPs is assumed to be the same as the base fluid velocity. The "frozen" boundary condition is considered for the particles over the artery wall surface, so particles will stick to the wall as they touch it.

## 2.3. Governing equations

### 2.3.1. Fluid phase

This work modeled blood as the continuous phase assuming laminar, pulsatile, incompressible, non-Newtonian flow without magnetization. Since the volume fraction of the discrete phase is sufficiently low – less than  $10^{-6}$  – so, the effect of the particles on the base fluid is negligible [37], while the flow influences particles' motion. This kind of coupling is called the one-way coupling used in this work [54]. The continuity and momentum equations are written as follows [55,56]:

$$\nabla \cdot \mathbf{u} = 0 \quad (2)$$

$$\rho \left( \frac{\partial \mathbf{u}}{\partial t} + (\mathbf{u} \cdot \nabla) \mathbf{u} \right) = -\nabla p + \mu \nabla^2 \mathbf{u} \quad (3)$$

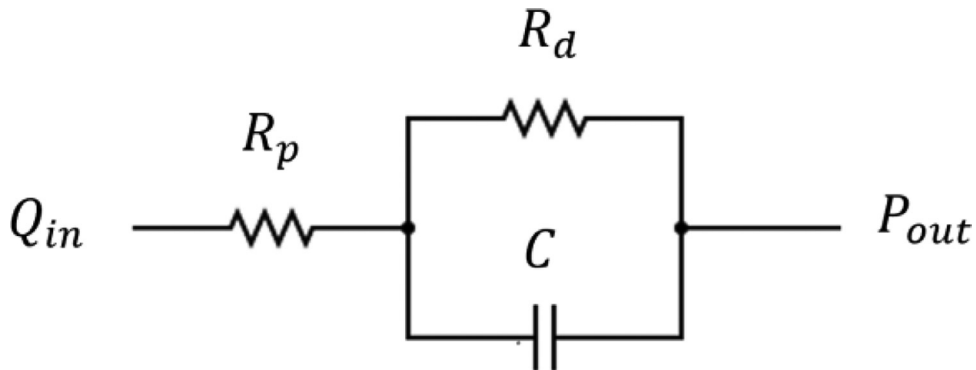


**Fig. 3.** Three-element Windkessel boundary condition circuit diagram.

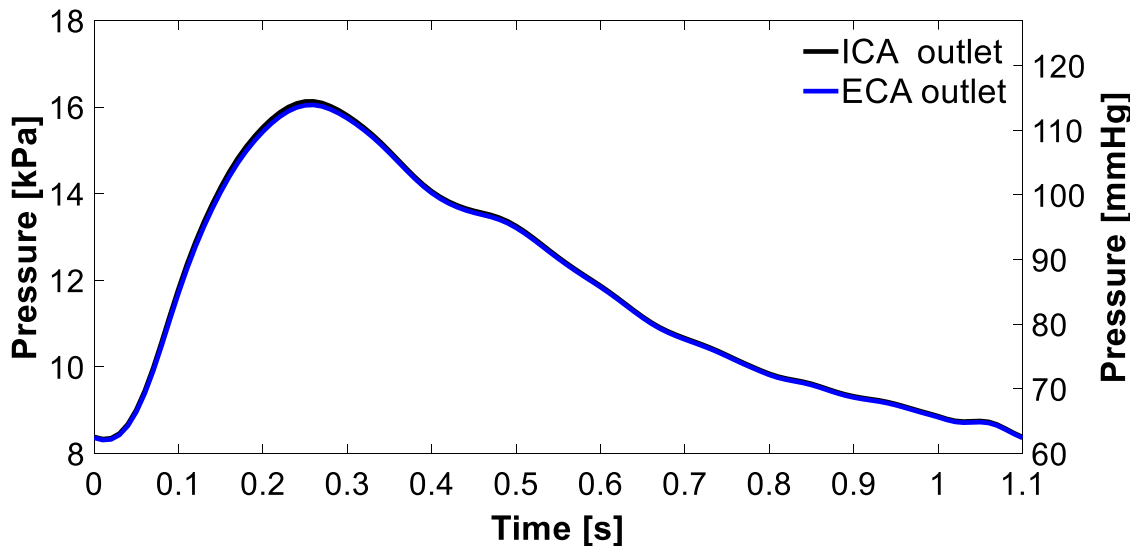


**Fig. 4.** ICA and ECA outlet pressure boundary condition.

**Table 4**  
Fluid properties [2].

Parameter	Value
$\rho$	1060 [kg/m <sup>3</sup> ]
$\mu_\infty$	0.0035 [kg/m·s]
$\mu_0$	0.0560 [kg/m·s]
$\lambda$	3.313 [s]
$n$	0.3568

In which  $\mathbf{u}$  is fluid velocity vector,  $\rho$  is the density of blood,  $p$  is the pressure, and  $\mu$  is the dynamic viscosity, which according to the possible important role of the non-Newtonian blood rheology [57,58] is presented by the non-Newtonian Carreau model as follows [2]:

$$\mu(\dot{\gamma}) = \mu_\infty + (\mu_0 - \mu_\infty)(1 + (\lambda\dot{\gamma})^2)^{\frac{n-1}{2}} \quad (4)$$

In the above relation,  $\dot{\gamma}$  is the strain rate,  $\mu_\infty$  is the infinite shear rate viscosity,  $\mu_0$  is the zero-shear rate viscosity,  $\lambda$  is the relaxation time, and  $n$  is the power index. The values of the mentioned parameters used in this work are given in Table 4.

### 2.3.2. Magnetic field

The magnetic field is generated by a permanent magnet and affects the particles' pathway. The Gauss's law equation is used to calculate the magnetic field in which  $\mathbf{B}$  is the applied magnetic

field [41].

$$\nabla \cdot \mathbf{B} = 0 \quad (5)$$

The stationary magnetic field around the permanent magnet is obtained from the following equation:

$$\mathbf{B} = \mu_0\mu_r(\mathbf{H} + \mathbf{M}) \quad (6)$$

in which,  $\mu_0 (4\pi \times 10^{-7} [\text{H/m}])$  is the magnetic permeability of vacuum,  $\mathbf{M}$  is the magnetization,  $\mu_r$  is the relative magnetic permeability of the surroundings, and  $\mathbf{H}$  is the induced magnetic field. As for the artery and the surrounding tissue, the magnetization is zero; therefore, the applied magnetic field is obtained from the following equation [44]:

$$\mathbf{B} = \mu_0\mu_r\mathbf{H} \quad (7)$$

### 2.3.3. Particle phase

MNPs and their movement are affected by several forces caused by the fluid, boundaries, other particles, and external affecting forces. These forces can be categorized as drag force, lift force, unsteady flow forces, Brownian motion force, thermophoretic force, forces due to magnetic or electrical fields, gravitational force, and so on [59,60]. The review by Mahian et al. [38] is helpful for more information about the mentioned forces and their sources.

A scaling analysis showing the order of magnitude for some of the mentioned forces is given in Table 5. In this table,  $\text{Re}_G$  is the shear Reynolds number,  $\chi$  is the density ratio,  $\text{Re}_p$  is the particle Reynolds number,  $\text{Pe}_p$  is the particle Peclat number,  $\text{Fr}$  is the particle Froude number, and  $\varepsilon$  is the dimensionless particle diameter

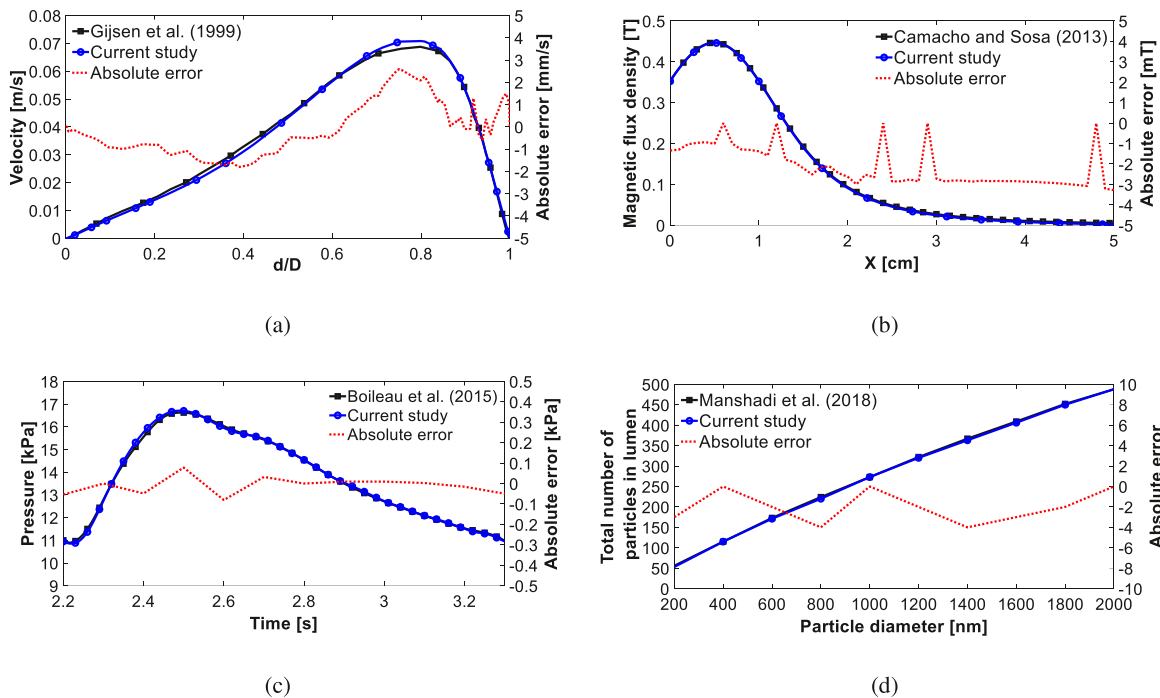


**Fig. 5.** Comparison of the current study results with those of other published works exhibiting: (a) velocity; (b) magnetic flux density; (c) pressure; and (d) the total number of captured particles.

**Table 5**  
Order of magnitude of forces induced by the base fluid acting on a particle [59].

Main force	Subdivided groups	Order of magnitude relative to particle inertia/drag
Drag force	Drag force	1
Lift force	Saffman lift force	$Re_G^{1/2}$
	Magnus lift force	$Re_G$
Unsteady flow forces	Added mass (virtual) force	X
	Pressure gradient force	X
	Basset history force	$Re_p^{1/2}$
Brownian force	Brownian force	$Pe_p^{-1/2}$
gravitational force	gravitational force	$(\varepsilon Fr^2)^{-1}$

**Table 6**  
Parameter values and properties of magnetite used in the present study [41].

Parameter	value
$\rho_p$	5230 [kg/m <sup>3</sup> ]
$X_p$	3.1
$d_p$	(200:200:2000) [nm]
$\rho_f$	1060 [kg/m <sup>3</sup> ]

[59]. The base fluid characteristics and  $Fe_3O_4$ (magnetite) particles properties are illustrated in Table 6 [41]. Because of the small size of particles and the greater density of them in comparison to the blood density, so  $Re_G, Re_p, Pe_p$ , and  $Fr \ll 1$ . Also, the density ratio is small, therefore the lift force, the unsteady flow forces, and the Brownian motion force are negligible. It's assumed that the blood temperature during MDT is constant, so the thermophoretic force is also insignificant. Eventually, the drag and the magnetophoretic forces are the dominant forces. In the Lagrangian frame of reference, Newton's second law for a single particle is as follows:

$$\frac{d\mathbf{u}_p}{dt} = \mathbf{F}_D + \mathbf{F}_M \quad (8)$$

where  $\mathbf{F}_D$  and  $\mathbf{F}_M$  are the drag and the magnetophoretic forces per unit mass of the particle, respectively, and  $\mathbf{u}_p$  is the particle velocity.

**2.3.3.1. Drag force.** The drag force on a spherical particle is given by the well-known Schiller-Naumann relation, which is defined as follows [44]:

$$\mathbf{F}_d = \frac{3\mu C_D Re_p}{4\rho_p d_p^2} m_p (\mathbf{u} - \mathbf{v}) \quad (9)$$

$$C_D = \frac{24}{Re_r} (1 + 0.15 Re_r^{0.687}) \quad (10)$$

$$Re_r = \frac{\rho |\mathbf{u} - \mathbf{v}| d_p}{\mu} \quad (11)$$

In which  $\rho_p$  is the particle density,  $d_p$  is the particle diameter,  $\mu$  is the dynamic viscosity,  $C_D$  is the drag coefficient,  $Re_p$  is the particles Reynolds number,  $m_p$  is the particle mass,  $\mathbf{u}$  is the blood velocity vector, and  $\mathbf{v}$  is the particle velocity vector.

**2.3.3.2. Magnetophoretic force.** For a spherical superparamagnetic particle moving in a steady magnetic field, the magnetophoretic force is defined as [41]:

$$\mathbf{F}_M = 2\pi \mu_{r,b} \mu_0 r^3 K \nabla \mathbf{H}^2 \quad (12)$$

$$K = \frac{\mu_{r,p} - \mu_{r,b}}{\mu_{r,p} + 2\mu_{r,b}} \quad (13)$$

In the above relations  $\mathbf{H}$  is the external magnetic field,  $\mu_0$  is the magnetic permeability of vacuum,  $\mu_{r,b}$  is the magnetic permeability of blood,  $r$  [m] is the particle's radius,  $\mu_{r,p}$  is the particle's magnetic permeability.  $K$  is the Clausius-Mossotti factor ( $-0.5 \leq K \leq 1.0$ ), which is a scale of the magnitude of the magnetophoretic force and its direction [41].

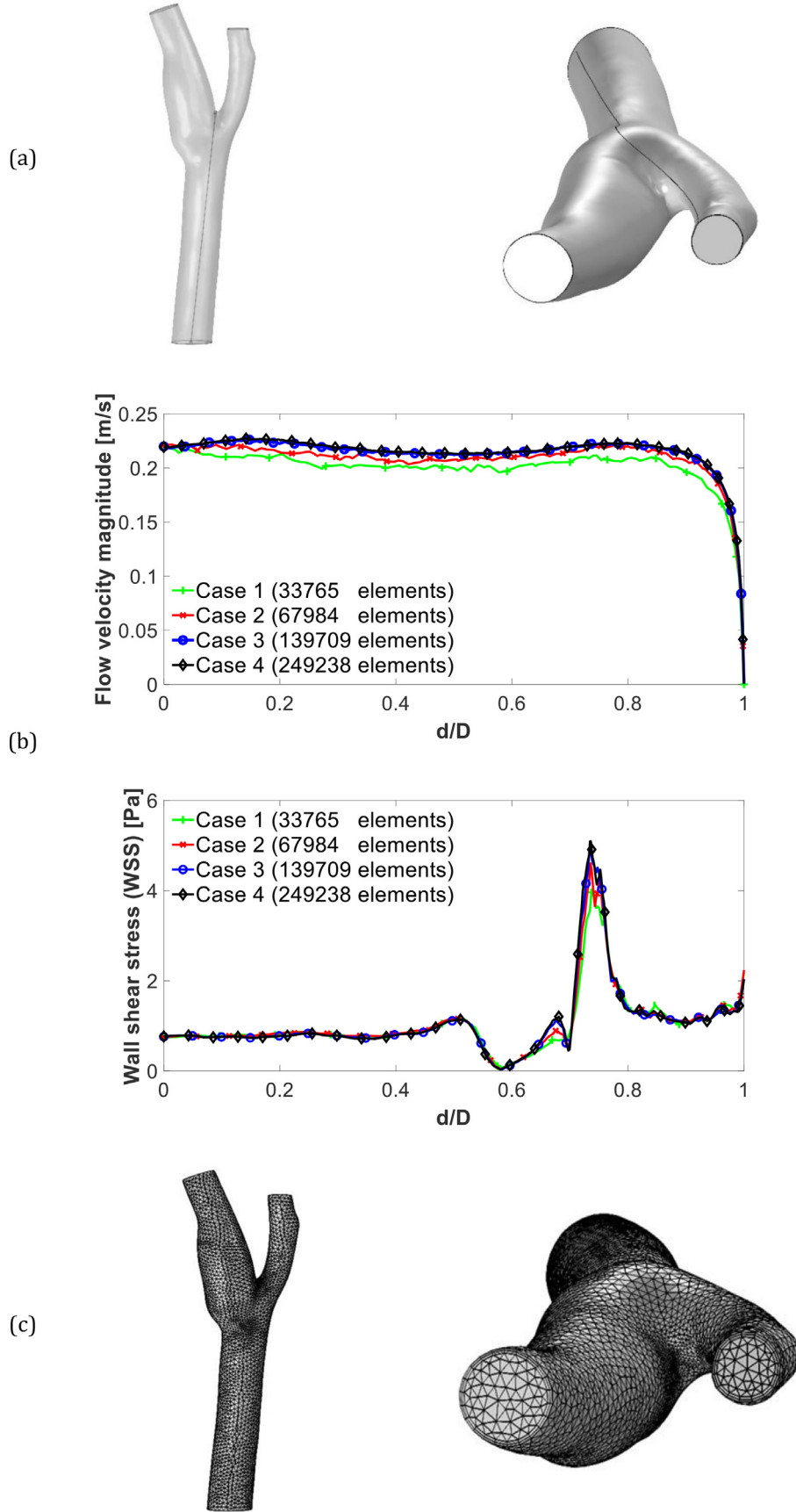


**Fig. 6.** (a) The line segments used to perform the mesh independence study, (b) comparison of the numerical results with different grids showing velocity and WSS, and (c) the grid generated to resolve the problem.

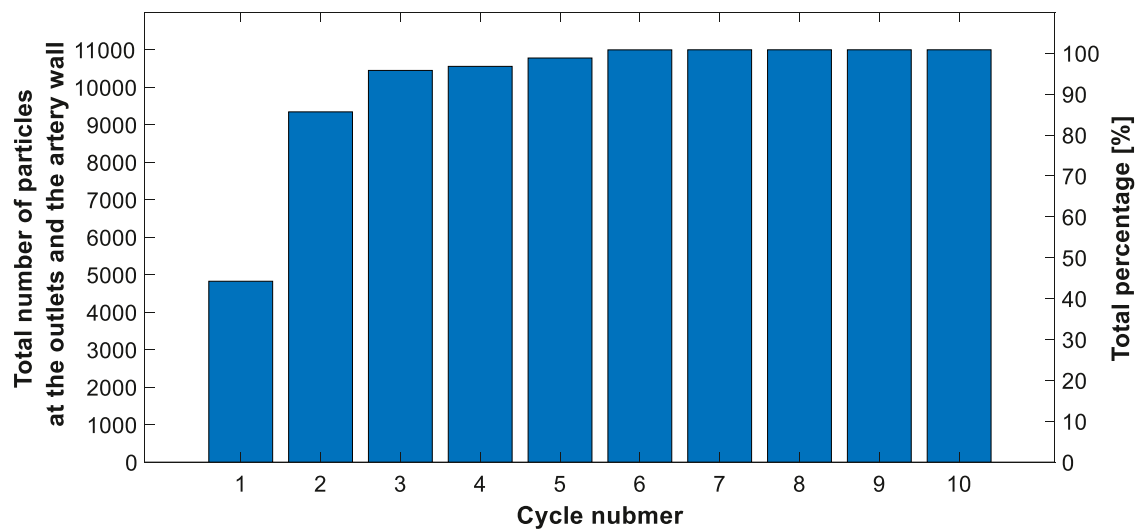


**Fig. 7.** Hear beat cycle independence for the computational time in this study.

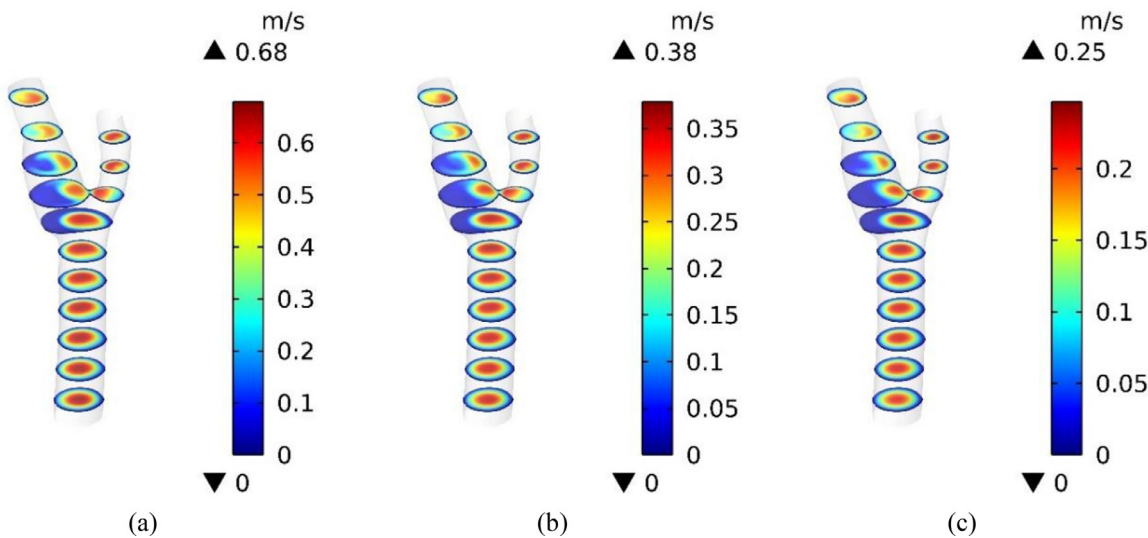


**Fig. 8.** Blood velocity field at (a) the peak systole; (b) the average magnitude in a cycle; and (c) the early diastole.

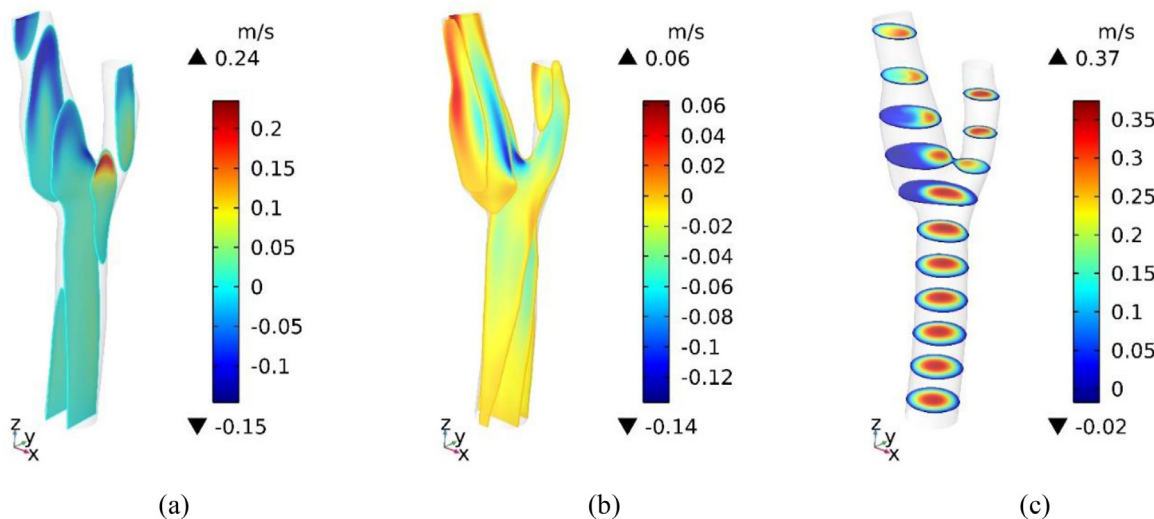


**Fig. 9.** Blood velocity components in (a) X-direction; (b) Y-direction; and (c) Z-direction.

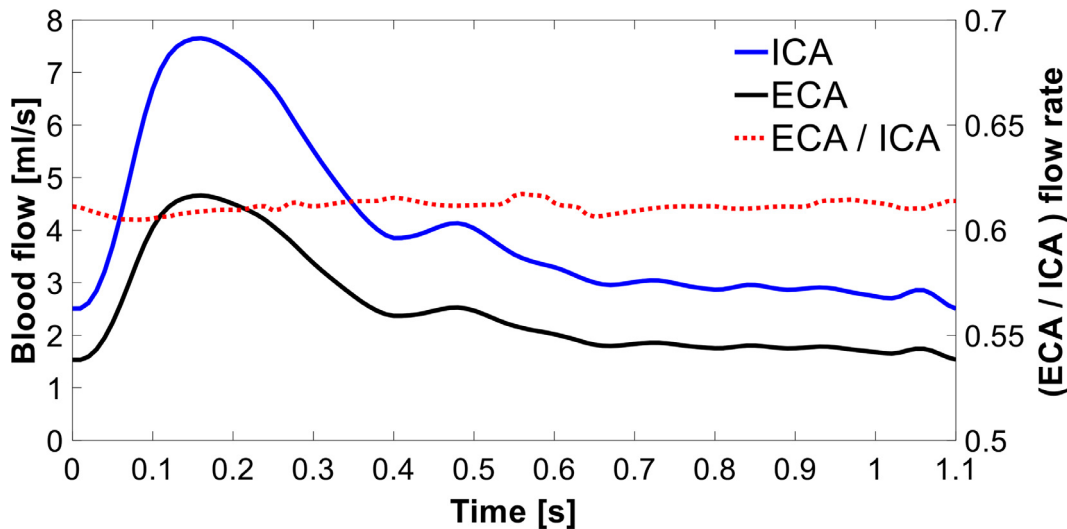


Fig. 10. Blood flow rate at ICA and ECA outlets and their ratio.

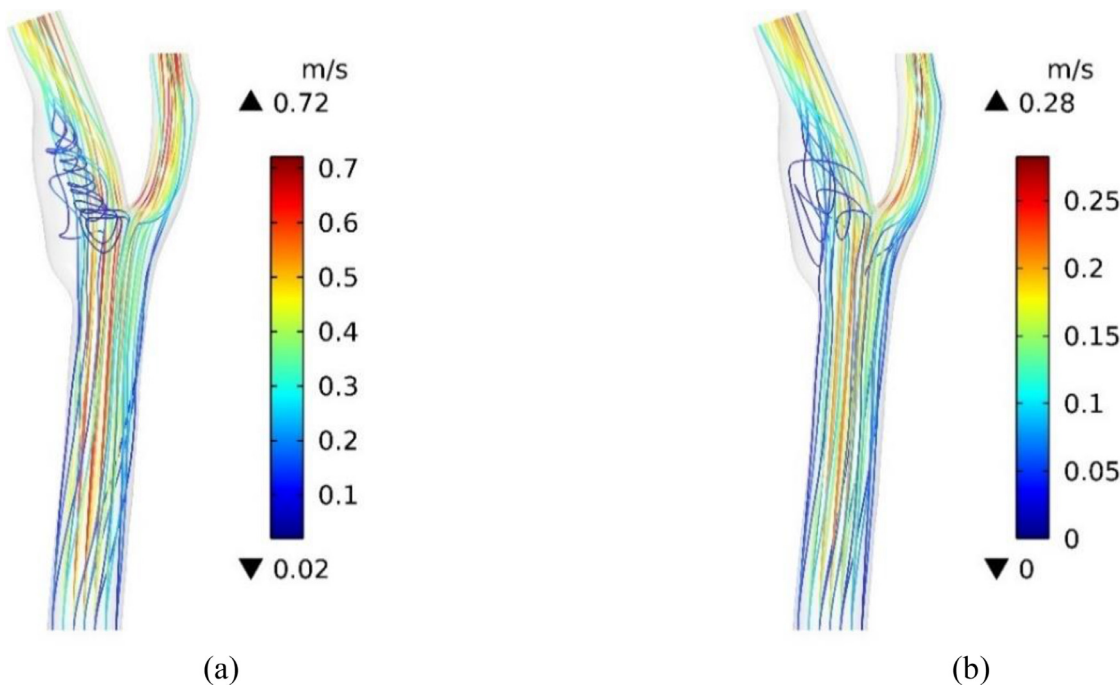
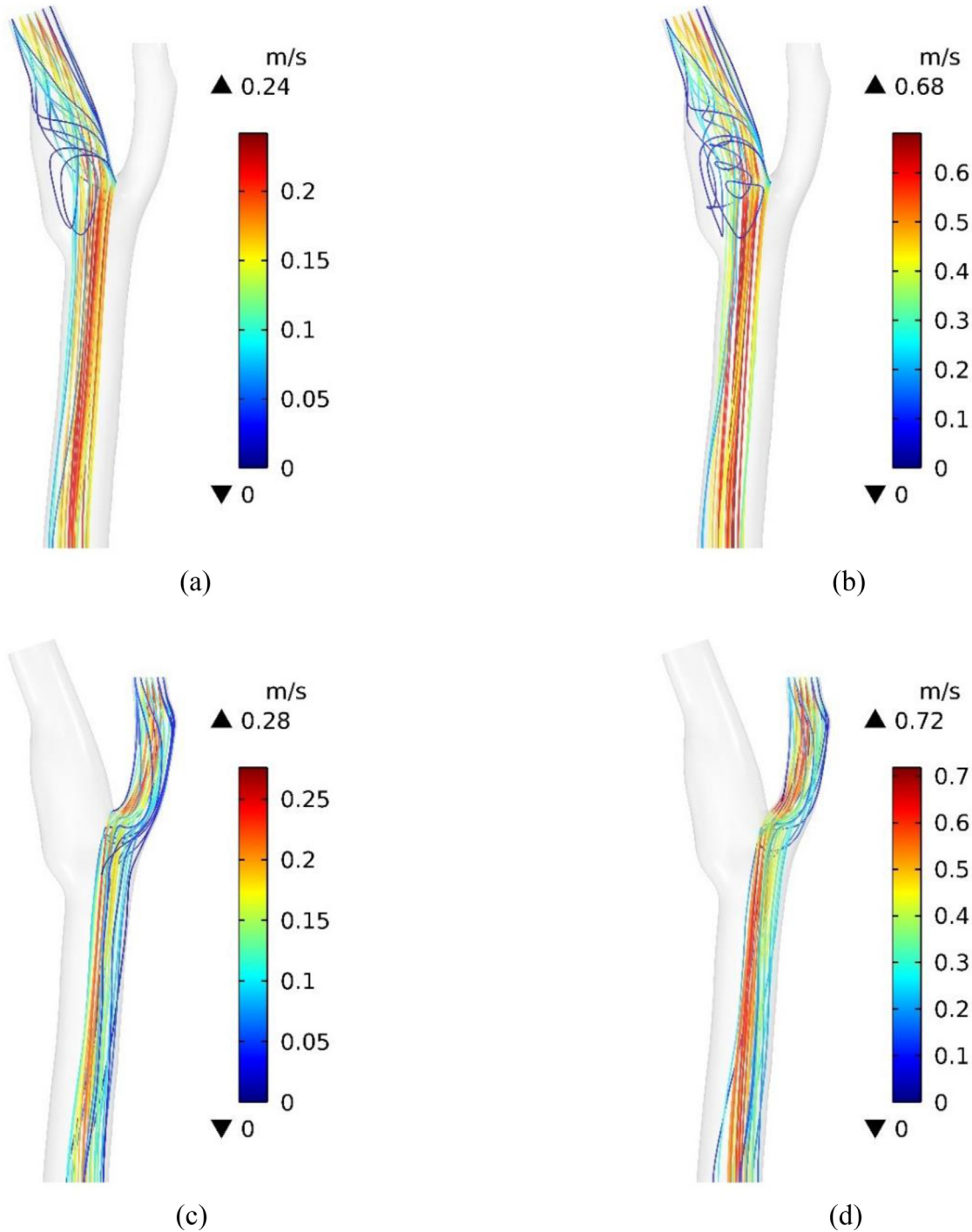


Fig. 11. Flow streamlines; at (a) the peak systole; and (b) the early diastole.

#### 2.4. Numerical method

Numerical simulation is carried out using the finite element method (FEM). The governing partial differential equations (PDEs) include four physics which are solved during three study steps by COMSOL Multiphysics 5.6. The first two physics (i.e., the Winkessel boundary conditions coupled with the non-Newtonian fluid dynamics), which are used to solve the velocity and pressure fields simultaneously, are discretized using linear elements (P1+P1) and discontinuous quadratic elements. A MUMPS (multi-frontal massively parallel sparse) direct solver is used to obtain the velocity and pressure fields. The third physic (i.e., the magnetic field) is applied to the problem using the “magnetic fields, no currents (MFNC)” physic and is discretized as a quadratic element. This step is solved using the conjugate gradient (CG) solver with an appropriate preconditioner. Finally, the so-called “flow particle tracing

(FPT)” physic is added to the model and is solved using the PARDISO (parallel direct solver). Relative tolerances used to satisfy the convergence criteria for the three-mentioned steps are considered as  $10^{-4}$ ,  $10^{-3}$ , and  $10^{-5}$ , respectively. Unstructured triangular, rectangular, prismatic, and tetrahedral elements (majorly tetrahedral grids for the surface and volume of the artery) are used to generate the computational grid. An adaptive time-stepping scheme is utilized in all the steps to maintain the desired relative tolerance. For the first and second steps, the 2<sup>nd</sup> order backward differentiation formula (BDF) method is applied. The steps taken by the solver are chosen to be free and strict, respectively. The generalized alpha method with strict steps taken by the solver is utilized to compute the solution for the particle tracing step. Compared to BDF, the generalized alpha method has much less damping and is thereby more accurate. For the same reason, the generalized alpha method is also less stable [61,62].



**Fig. 12.** Streamlines originated from the CCA inlet and ended to ICA or ECA at (a, c) the early diastole; (b, d) the peak systole.

## 2.5. Validation

To verify the numerical results, all the applied physics are simulated, and their results are compared with those of published works. The work of Gijzen et al. [63] is used to validate the true-ness of the non-Newtonian blood flow using the Carreau-Yasuda model, as depicted in Fig. 5(a). In addition, the analytical results of Camacho and Sosa [64] are used to verify the steady-state magnetic field simulation results around a cylindrical magnet (see Fig. 5(b)). Also, the pressure of CCA is obtained numerically by using the RCR boundary condition and is compared with the results

of Boileau et al. [50], as exhibited in Fig. 5(c). Finally, for the validation of the particle movement solver, the numerical results of Manshadi et al. [44] are used where drug delivery in a rectangular channel is simulated in the presence of a 1.5 T magnetic field (see Fig. 5(d)).

## 2.6. Grid independence

A mesh independence study is performed to reduce the computational cost while achieving accurate grid-independent results. The velocity and wall shear stress (WSS) are reported for differ-

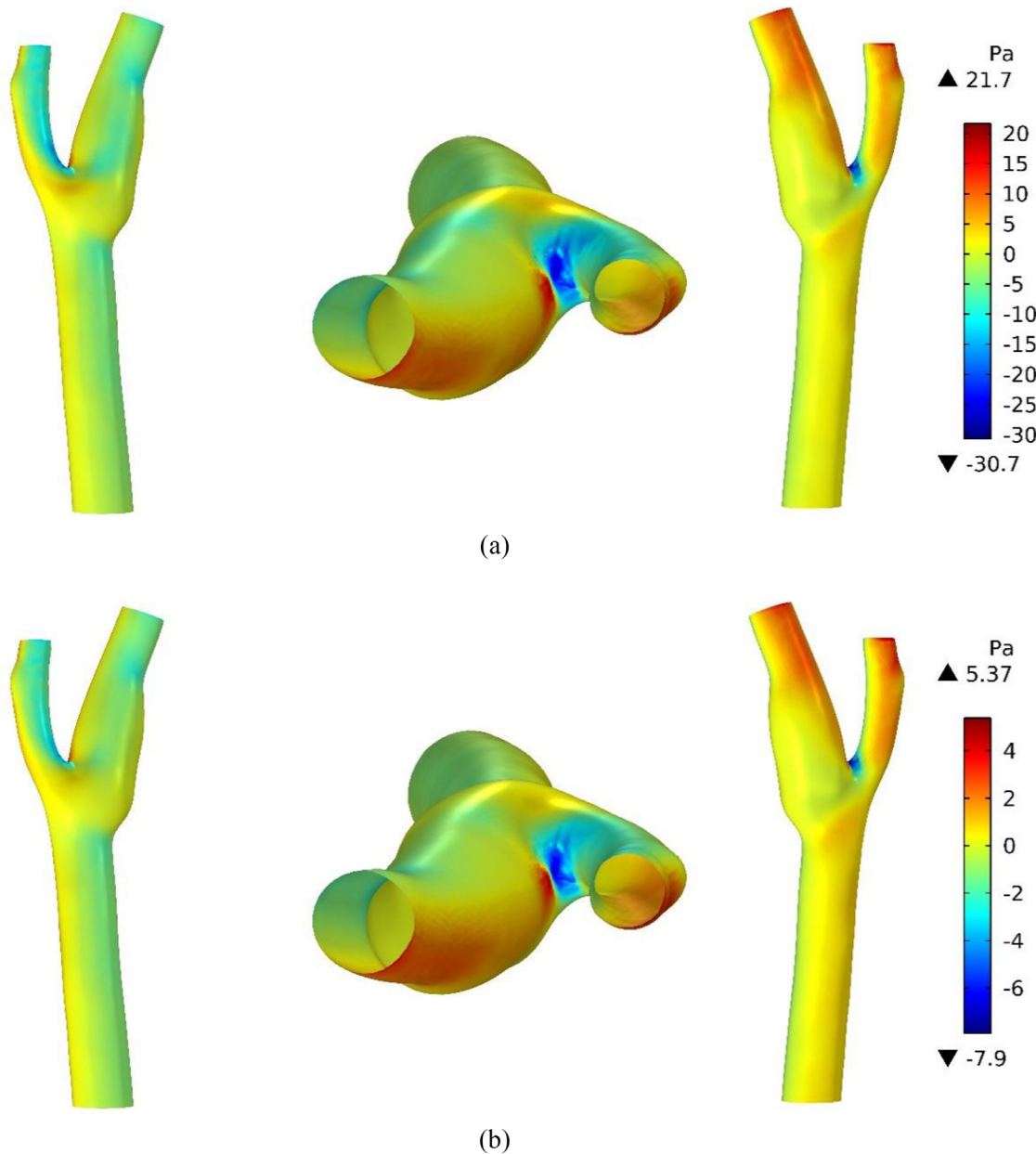


**Fig. 13.** WSS contour from different views at (a) peak systole; and (b) early diastole.

ent grids to check the grid independence. The velocity is reported across the line segment between the CCA inlet center point and bifurcation apex point, and the WSS is presented on a line segment shown in Fig. 6(a). According to the results illustrated in Fig. 6(b), the case with 139709 elements, as depicted in Fig. 6(c), could provide accurate and independent results from the computational grid.

#### 2.7. Time independence

According to the time-dependent nature of particle-tracing studies, selecting an appropriate simulation time is essential to balance the computational cost and the accuracy of the results. For this reason, particle tracing is done in ten cycles of heartbeats without a magnetic field. At the end of each cycle, the summation of the particles at the ICA and ECA outlets and on the artery wall is evaluated, as illustrated in Fig. 7. As can be seen, at the end of the sixth cycle, almost 100 percent of the released particles have

reached the outlets or are stuck to the wall. Accordingly, six cycles (the computational time range of 0 to 7.7 seconds) are considered. In the first cycle, the flow and magnetic fields reach a stable point, and then the particles are released.

### 3. Results and discussion

An appropriate analysis of MDD in the arteries needs a good perspective about the base flow characteristics and its effects on the vessel wall to determine the proper magnet placement and the regions prone to some CVDs. Hence, first, blood flow analysis results are explained, and some important parameters about the arteries' health are introduced. Then MDD is performed to conduct the drug toward the desired path better, implementing different arrays of permanent magnets. This work applies the safe magnetic field to the carotid artery bifurcation. Also, the drug delivery results in the presence and absence of the magnetic field are compared and analyzed.

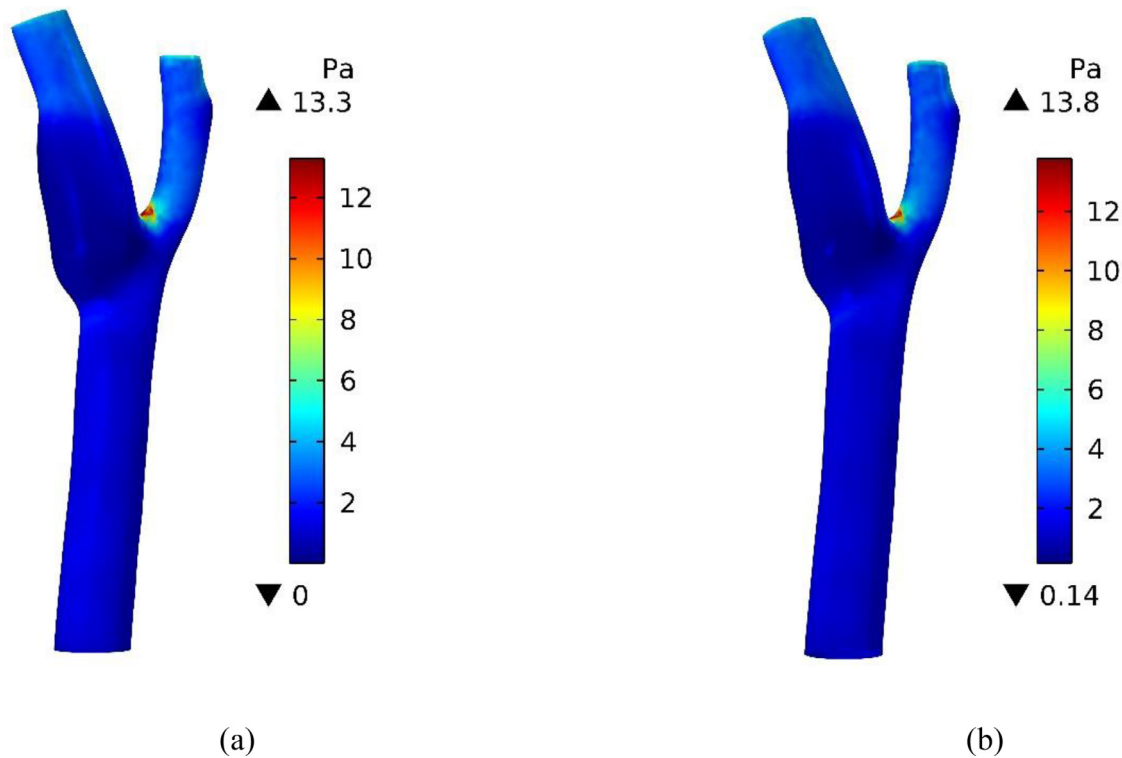


**Fig. 14.** Contours of (a) TAWSS; and (b)  $\tau_{\text{mag}}$ .

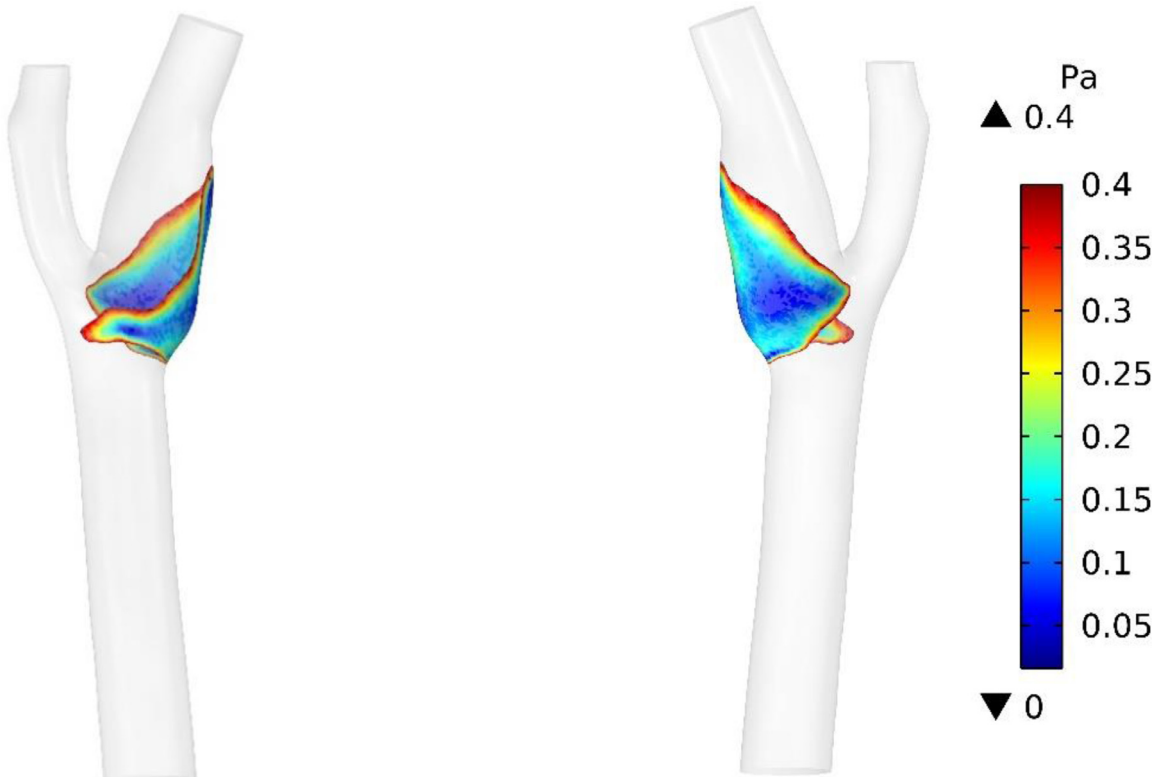


**Fig. 15.** Prone regions to atherogenesis ( $\text{TAWSS} < 0.4 \text{ Pa}$ ).

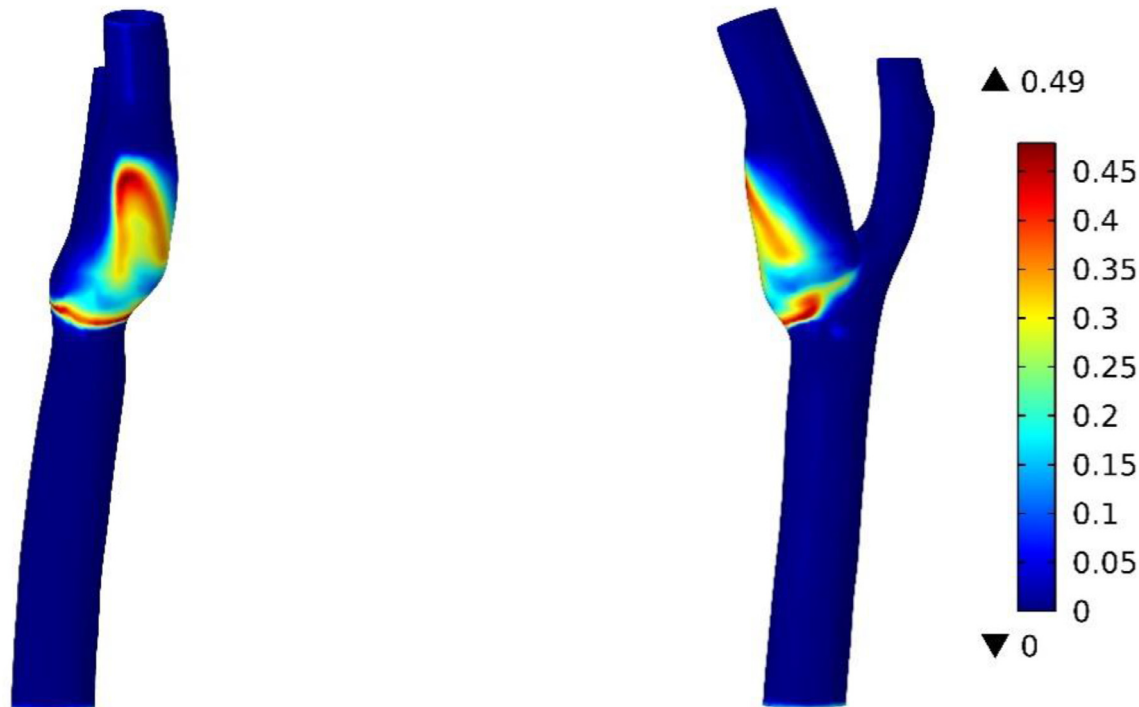


Fig. 16. OSI contours.

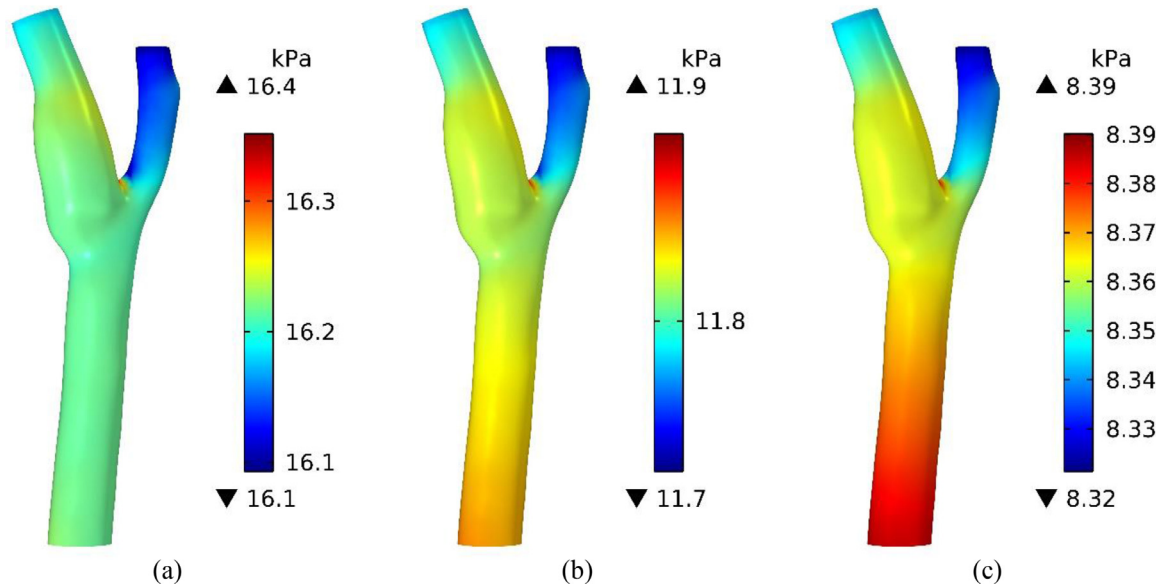


Fig. 17. Pressure contours at (a) the maximum; (b) the average; and (c) the minimum pulse pressure times during a cycle.

### 3.1. Fluid phase

To steer the particles to the desired location in MDD and MDT, the ability to overcome the hydrodynamic drag force produced by the blood flow is the main principle that is proportional to the blood velocity. So, it is essential to become aware of the blood velocity in the artery to perform proper drug targeting. The blood velocity field magnitude in horizontal slices at different times is illustrated in Fig. 8. In the CCA region, the velocity magnitude profile is almost symmetrical, but as it reaches the carotid bifurcation due

to the asymmetric expansion of the artery, the profile changes. The flow divides into two different regions of ICA and ECA at the apex zone. As a result, the velocity magnitude profile becomes asymmetric, especially in the ICA due to the existence of the carotid sinus bulb, and the velocity magnitude becomes higher in the interior side of the artery branches than the CCA region, where the higher velocity magnitude region is in the middle of the artery. The velocity becomes more symmetrical as the flow reaches the outlets, particularly ECA. To have a more detailed view of the blood velocity, the flow direction is essential besides the magnitude of

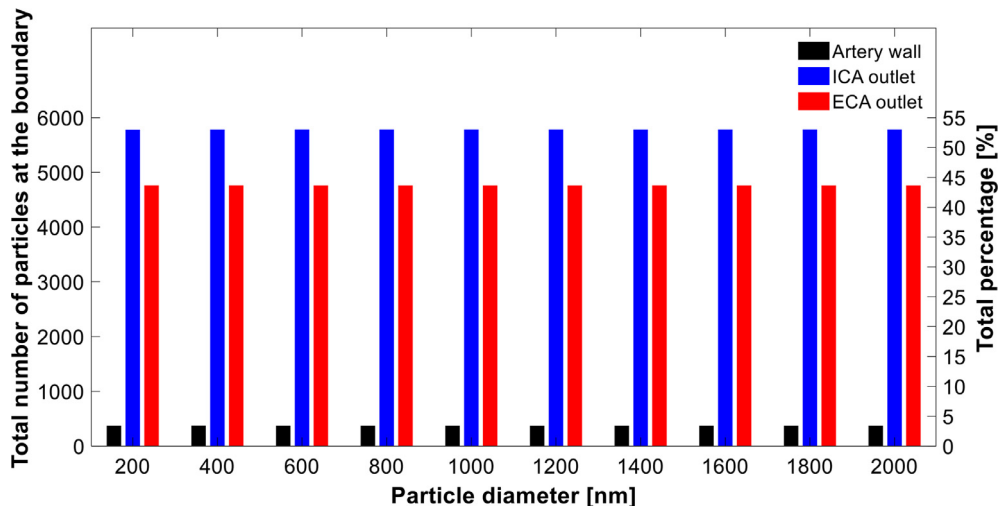


Fig. 18. Total number of particles reaching the ICA and ECA outlets or deposited on the wall after natural drug delivery.

the flow. So, to show the direction of the flow, the average velocity field components during one cardiac cycle in different directions are shown in Fig. 9. As shown, in the CCA region, the blood flow velocity does not have noticeable values in the X and Y directions, so it can be justified that the flow is unidirectional in the CCA zone. In the ICA zone, reverse axial velocity is observed because of low momentum regions, implying blood circulation in these areas.

The blood flow rates at the outlets are illustrated in Fig. 10. The average ECA to ICA blood flow ratio is 0.61, which is in good agreement with the results of Onaizah et al. [65]. Some streamlines of the blood flow originating from the CCA inlet are shown in Fig. 11 to clarify particle path lines and show the regions with circulating flow. Blood flow at the bifurcation and in the ICA sinus bulb has recirculating areas. While, in the CCA, ECA, and after the sinus bulb region in the ICA, blood flow becomes unidirectional. It is worth mentioning that the recirculation is more intensive at peak systole compared with early diastole, in agreement with the results of Lopez et al. [66]. From the drug delivery point of view, it is vital to know the portion of the streamlines and their locations end to the ICA or ECA outlets, as illustrated in Fig. 12. This figure shows that the streamlines in the ICA side of the CCA region mostly enter the ICA outlet. The same fact is true about the streamlines on the ECA side. Accordingly, to impact the particles at each side, it would be better to put the magnets at that side of the wall artery.

Important parameters like wall shear stress (WSS), oscillatory shear index (OSI), and pressure are investigated to identify the arteries' regions that are prone to CVDs. WSS is the friction force per unit area applied by circulating blood column on the interior wall of the artery and is accounted by the following equation [67]:

$$\tau_{wall} = \mu \cdot ((\nabla \times \mathbf{u}) \cdot \vec{n}) \quad (14)$$

where  $\vec{n}$  is the normal unit vector of the tangential plane to the vessel wall. WSS at the peak systole and early diastole is shown in Fig. 13. As can be seen, the maximum WSS happens near the bifurcation apex due to the high-velocity gradients in this region. Also, the lowest values of WSS exist at the carotid sinus bulb, which agrees with the results from Nagargoje and Gupta [68] and makes this place prone to plaque accumulation [69]. It has been reported that a WSS of above 40 Pa can harm the endothelial cells, and a WSS of more than 100 Pa results in detachment of endothelial cells and formation of clots [70]. OSI is another mechanical factor related to WSS deflection from the average due to flow disturbance over a cardiac cycle [71]. Time average wall shear stress magnitude

(TAWSS) and time mean magnitude of the wall shear stress ( $\tau_{mag}$ ) are two important parameters that OSI is defined by them. These parameters are formulated using the following equations respectively [70,72]:

$$TAWSS = \left| \frac{1}{T} \int_0^T \tau_{wall} dt \right| \quad (15)$$

$$\tau_{mag} = \frac{1}{T} \int_0^T |\tau_{wall}| dt \quad (16)$$

In which  $T$  [s] is the pulse period time and  $\tau_{wall}$  [Pa] is the instantaneous WSS. Fig. 14 illustrates the TAWSS and  $\tau_{mag}$ . Low value of TAWSS (lower than 0.4 Pa) shows the locations where Neointima thickening takes place [70,73], as shown in Fig. 15. The sinus bulb is the most likely place to have atherosclerosis in the carotid artery. OSI is obtained by the following equation [72]:

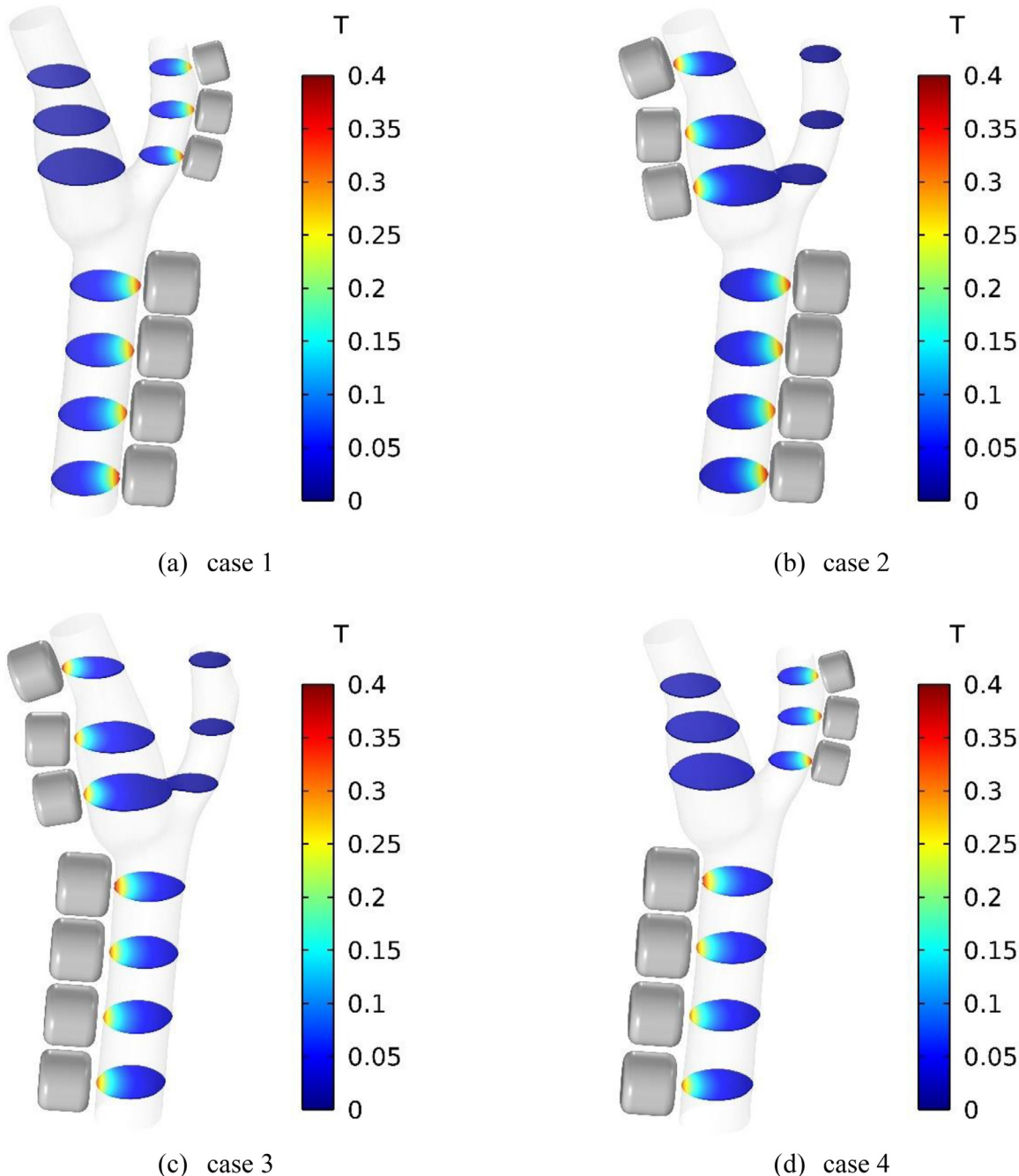
$$OSI = \frac{1}{2} \left( 1 - \frac{TAWSS}{\tau_{mag}} \right) \quad (17)$$

Fig. 16 demonstrates OSI contour at different views of the carotid artery. OSI ranges between 0 (pure unidirectional flows) and 0.5 (totally oscillatory flows). As seen, at the start of bifurcation at the ICA side and in the regions of the exterior side of the sinus bulb, OSI has the highest values, which makes these places prone to endothelial dysfunction and atherogenesis [74].

Stroke is usually caused by high blood pressure with the subsequent rapture of the arteries. Therefore, pressure contours on the artery wall and at different times are illustrated in Fig. 17. As can be seen, pressure, unlike the other studied parameters, does not significantly vary at different wall regions. At the same time, the maximum value occurs at the bifurcation due to the presence of the stagnation point. In addition, the pressure values on the ICA wall are higher than those of the ECA wall.

### 3.2. Particle phase

Firstly, to investigate natural drug delivery in the carotid artery without any external magnetic field, the drug particles are released from the CCA inlet with the initial velocity of the blood flow. After six cycles, the total number of particles at the wall and each outlet are counted. Fig. 18 illustrates the number of deposited particles on the wall and the number of particles reaching the ECA and ICA



**Fig. 19.** Different magnet arrangements and the generated magnetic field.

outlets, considering particles with different diameters. As can be seen, the effect of particle diameter on the results is not noticeable.

Four different arrangements of cylindrical permanent magnets with fillet edges (as illustrated in Fig. 19) are used to investigate the effect of the magnetic field on drug delivery performance. These magnets can be considered either as implanted permanent magnets or could be assumed as representative of an external magnetic field generator. The physical properties of the magnets are expressed in Table 7. The size of magnets is proportional to the artery size at each branch, and the generated magnetic field does not exceed 0.4 T to guarantee safe treatment. The total number of particles reaching the ICA and ECA outlets or deposited on the artery wall is presented in Fig. 20. The drug delivery efficiency

increment (DDEI) parameter is defined to check and compare the performance of each arrangement. DDEI is defined as the overall particle entrance percentage increase to the desired outlet plus the overall particle percentage entrance reduction at the undesirable outlet compared to the natural drug delivery results and is shown in Fig. 21. To compute the DDEI parameter, ICA is considered the desirable outlet for cases 1 and 2, while for cases 3 and 4, the ECA is the target outlet.

As shown in Fig. 20, in cases 1 and 2, the total number of particles reaching the ECA outlet decreases due to the magnets on the right-hand side of the CCA. Especially in case 1, the decrement becomes more intensive due to the magnets at the ECA side that absorb the particles moving towards the ECA outlet. Accord-

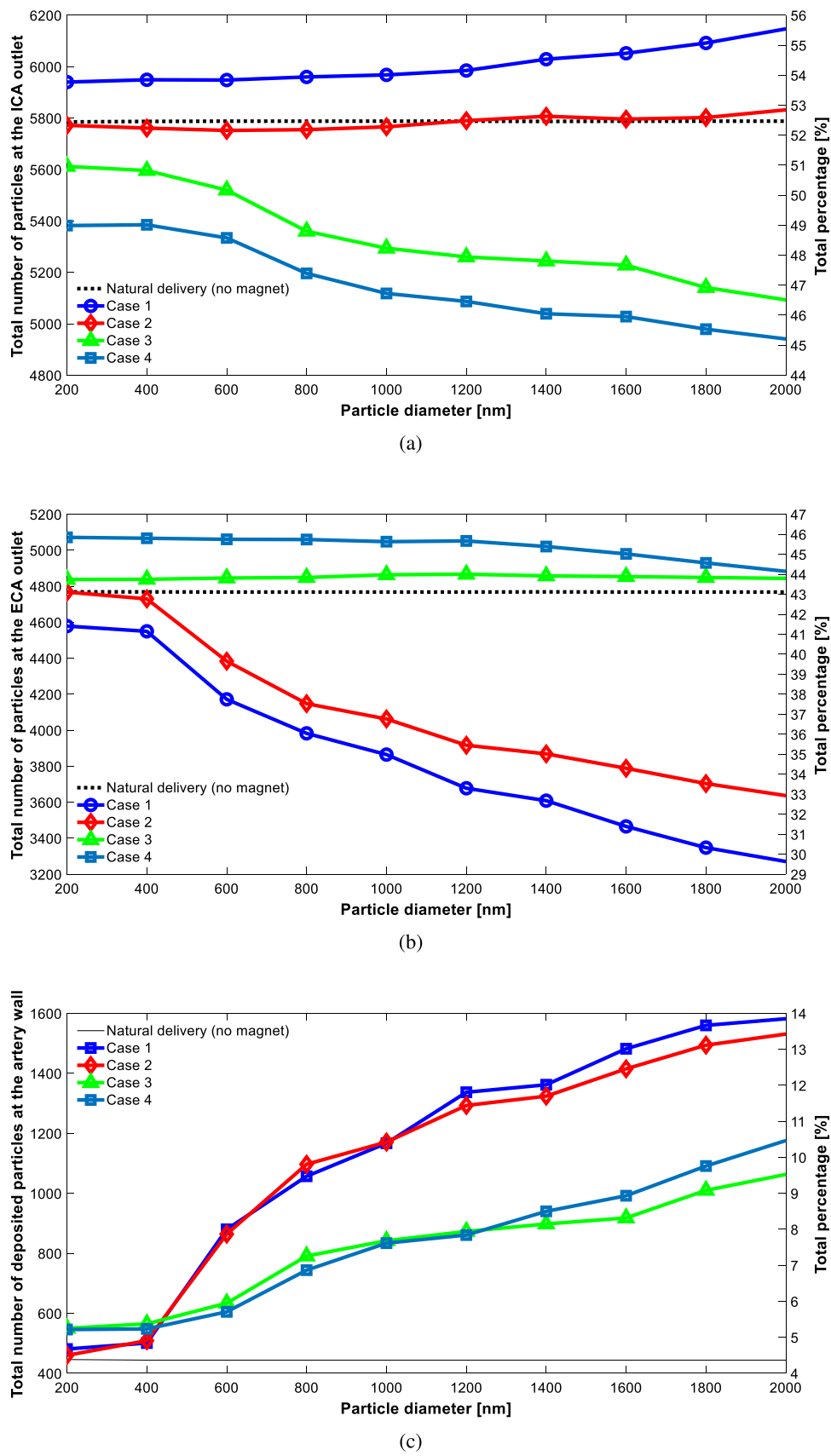


**Fig. 20.** Total number of particles reaching (a) ICA outlet; (b) ECA outlet; and (c) depositing on the artery wall and comparing them with natural drug delivery (Case 0).

**Table 7**  
Physical and magnetic properties of the applied magnets.

Location	Radius [mm]	Height [mm]	Fillet radius [mm]	Magnetization [A/m]
CCA	3	5	1	$10^6$
ICA	2.5	4	0.75	$10^6$
ECA	2	3	0.5	$10^6$

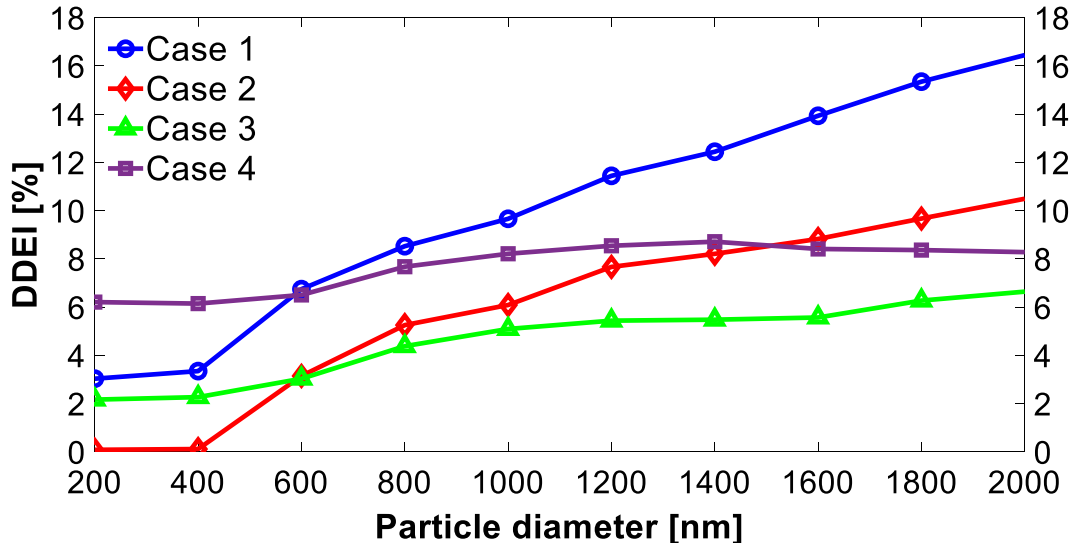


**Fig. 21.** DDEI for cases 1 and 2, where the ICA outlet is the desired outlet; and cases 3 and 4 in which the ECA outlet is the target.

ingly, the total particles at the ECA outlet in case 1 are lower than those in case 2. In these cases, the CCA magnets absorb the adjacent particles while slightly deviating the path line of the particles on the other side. Hence, the particles move toward the centerline and end to the ICA outlet. Accordingly, the number of particles at the ECA outlet decreases, and simultaneously, the total number of particles at the ICA branch outlet increases. In case 2, due to the existence of ICA magnets, some particles would stick to the artery's wall. Hence, the ICA magnets would thwart the effect of the CCA magnets for increasing the number of particles at the ICA outlet.

For cases 3 and 4, the total number of particles at the ICA outlet decreases due to the existence of CCA magnets. In case 3, the ICA magnets are placed near the sinus bulb region. As a consequence, the magnets at the ICA region are not as effective as case 4. For case 4, due to the presence of ECA magnets (especially the first one), low-velocity particles at the bifurcation area will deviate toward the ECA. Therefore, the total number of particles at the ICA outlet is lower in case 4 compared to case 3. In the same manner as cases 1 and 2, the CCA magnets absorb some particles and deviate them toward the ECA outlet. Hence, in cases 3 and 4, the total number of particles at the ECA outlet increases compared to the natural delivery case (no magnet). Obviously, for case 4, the total number of particles reaching the ECA outlet declines by increasing the particles' diameter. Increasing the particles' diameter can strengthen the effect of the ECA magnet on the particles. Hence, low-velocity particles will be absorbed with a resulting decrement in the total number of particles at the ECA outlet.

As shown in Fig. 20(c), in cases 1 and 2, the number of deposited particles is remarkably higher than cases 3 and 4. It can be caused by the artery curvature in the CCA region, which makes the pathlines towards the right side of the CCA. Also, in cases 1 and 4, because of the existence of the ECA magnets, the wall ab-

sorption of the particles is higher than cases 2 and 3, respectively. This shows that the magnets on the ECA branch are more dominant than the magnets on the ICA artery side due to the smaller diameter of the ECA branch and the existence of blood recirculation zones at the sinus bulb in the ICA region.

Observing the DDEI in Fig. 21 reveals that DDEI of cases 1 and 2 increases by increasing the particles' diameter continuously, such that case 1 always has a higher value than case 2. In these cases, the right-side placed CCA magnets become more and more dominant by increasing the particles' diameter, with a subsequent decline in the number of particles entering the ECA outlet. On the other side, the existence of the ICA magnets in case 2 prevents some particles from leaving the bifurcation at the ICA outlet and reduces the total number of particles at the desired outlet. DDEI for cases 3 and 4 shows that the difference between the DDEI of these cases decreases by increasing the particles' diameters, especially for particles larger than 1400 nm. Although the magnets at the ECA side are more effective than those at the ICA region, they are not completely dominant for small-sized particles; hence, the mentioned magnets help the particles enter the ECA branch and leave it as the target outlet. But, by increasing the particles' diameter, the ECA magnets become totally dominant and absorb most of the particles, resulting in the reduction of the overall particles at the ECA outlet. Fig. 22 depicts the final position of particles for the largest studied diameter to provide a better picture from the results. As shown, for the first and the second studied cases, there is no absorbed particle on the top side of the CCA compared to the neutral drug delivery case. The same point is true for cases 3 and 4 on the other side of the CCA. To describe it, the CCA side magnets guide the mentioned particles toward the desired outlet in all the cases. Also, the deposited particles aggregation in cases 1 and 4 are obviously higher than the other cases, revealing the domination of the ECA side magnets over those placed at the ICA side.

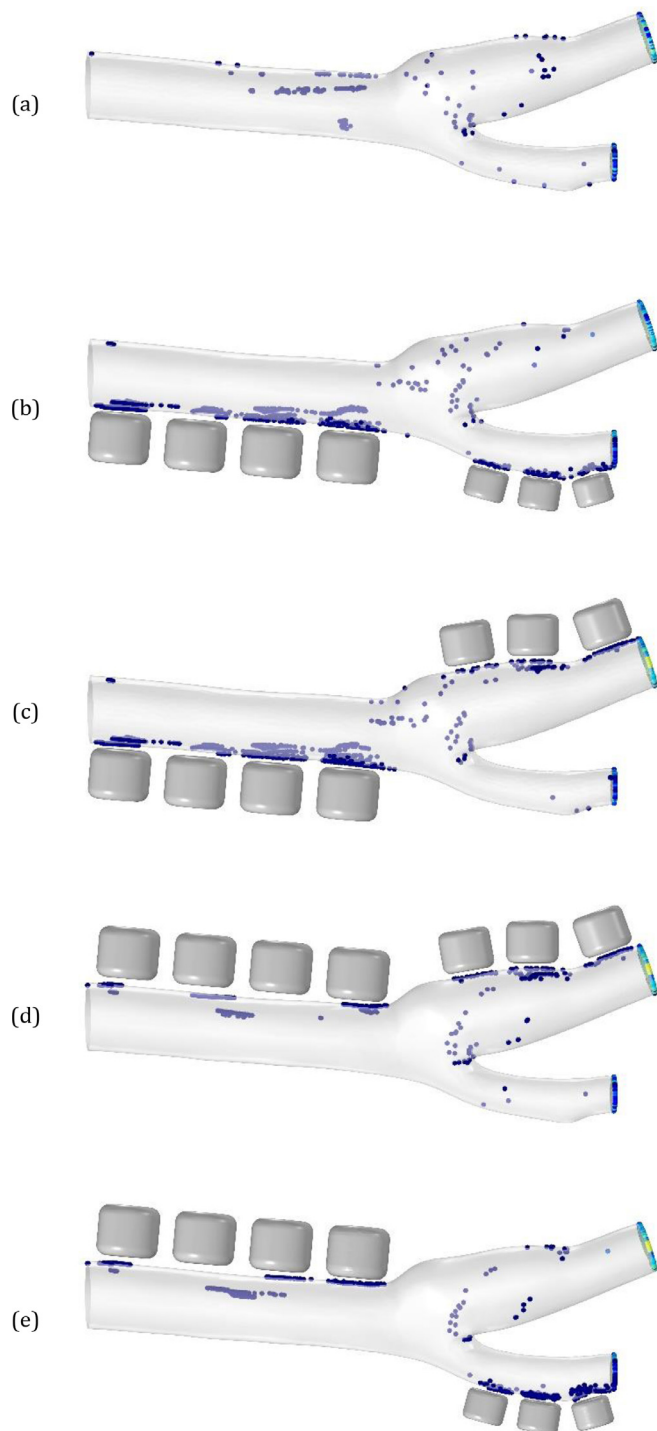


**Fig. 22.** The final position of particles (particles' diameter = 2  $\mu\text{m}$ ) in different cases for.

#### 4. Conclusions

In this work, by utilizing a realistic 3D CT-based carotid artery model and applying the physiological boundary conditions, blood flow in the carotid artery bifurcation is numerically studied. Regions with unidirectional and recirculation flows are found by investigating the velocity and pressure fields. Also, the most likely prone zones in the artery to cardiovascular diseases (CVDs) are identified by using wall shear stress (WSS) and oscillatory shear index (OSI) parameters. Magnetite particles with different diameters

are applied to perform drug-releasing. As a result, the particle diameter could not affect the natural drug delivery (no magnet), and the same results are obtained for the total final particles at each outlet. Applying four different magnet arrangements makes it possible to manipulate the number of the final particles at each outlet to conduct drug particles into the desired outlet. Proper selection of places for magnets implantation can be made through flow simulation results. The places with high OSI values (such as the sinus bulb with the recirculating flow) are not proper choices, while the areas with the unidirectional flow (like the CCA and ECA inlet) are appropriate choices. The primary outcomes can be summarized as follows:

- Blood flow is mainly unidirectional in CCA and ECA regions, while it has recirculation zones at the ICA branch, especially at the carotid sinus bulb.
- The WSS parameter has its highest value at the bifurcation apex and the lowest at the carotid sinus bulb, making these regions prone to CVDs.
- Although larger particles are more affected by the magnetic field, it does not always result in a higher drug delivery efficiency.
- DDEI is improved up to 6% to 17% for the smallest and largest investigated particles' diameter, respectively.

In the present study, the magnetic field in the bifurcation region was generated by considering different single implanted permanent magnets adjacent to the artery wall, which can represent an external magnetic field generator. Resolving the problem in the presence of an external magnetic field can trace the future direction of this research. Also, besides *in silico* simulations, *ex vivo* experimental studies a more precise insight into the MDT phenomenon.

#### Declaration of Competing Interest

The authors declare that they have no known competing financial interests or personal relationships that could have appeared to influence the work reported in this paper.

#### References

- [1] M. Ebadi, K. Buskaran, S. Bullo, M.Z. Hussein, S. Fakurazi, G. Pastorin, Drug delivery system based on magnetic iron oxide nanoparticles coated with (polyvinyl alcohol-zinc/aluminium-layered double hydroxide-sorafenib), Alexandria Engineering Journal 60 (1) (2021) 733–747, doi:[10.1016/j.aej.2020.09.061](https://doi.org/10.1016/j.aej.2020.09.061).
- [2] R.L. Hewlin, A. Ciero, J.P. Kizito, Development of a Two-Way Coupled Eulerian-Lagrangian Computational Magnetic Nanoparticle Targeting Model for Pulsatile Flow in a Patient-Specific Diseased Left Carotid Bifurcation Artery, Cardiovasc Eng Technol 10 (2) (2019) 299–313, doi:[10.1007/s13239-019-00411-8](https://doi.org/10.1007/s13239-019-00411-8).
- [3] C. Abugattas, A. Aguirre, E. Castillo, M. Cruchaga, Numerical study of bifurcation blood flows using three different non-Newtonian constitutive models, Appl. Math. Modell. 88 (2020) 529–549, doi:[10.1016/j.apm.2020.06.066](https://doi.org/10.1016/j.apm.2020.06.066).
- [4] I. Rukshin, J. Mohrenweiser, P. Yue, S. Afkhami, Modeling Superparamagnetic Particles in Blood Flow for Applications in Magnetic Drug Targeting, Fluids 2 (2017) 29, doi:[10.3390/fluids2020029](https://doi.org/10.3390/fluids2020029).
- [5] M.K.D. Manshadi, et al., Magnetic aerosol drug targeting in lung cancer therapy using permanent magnet, Drug Deliv. 26 (1) (Jan. 2019), doi:[10.1080/10717544.2018.1561765](https://doi.org/10.1080/10717544.2018.1561765).
- [6] H. Sodagar, A. Shakiba, H. Niazmand, Numerical investigation of drug delivery by using magnetic field in a 90-degree bent vessel: a 3D simulation, Biomech. Model. Mechanobiol. 19 (2020), doi:[10.1007/s10237-020-01337-0](https://doi.org/10.1007/s10237-020-01337-0).
- [7] H. Unterweger, et al., Development and characterization of magnetic iron oxide nanoparticles with a cisplatin-bearing polymer coating for targeted drug delivery, Int J Nanomedicine 9 (2014) 3659–3676, doi:[10.2147/IJNN.63433](https://doi.org/10.2147/IJNN.63433).
- [8] J. Ally, B. Martin, M. Behrad Khamesee, W. Roa, A. Amirfazli, Magnetic targeting of aerosol particles for cancer therapy, J. Magn. Magn. Mater. 293 (1) (2005), doi:[10.1016/j.jmmm.2005.02.038](https://doi.org/10.1016/j.jmmm.2005.02.038).
- [9] A. Ardalan, S. Aminian, A. Seyfaee, S. Gharehkhani, Effects of geometrical parameters on the capture efficiency of nanoparticles under the influence of the magnetic field in a stenosed vessel, Powder Technol. 380 (2021) 39–46, doi:[10.1016/j.powtec.2020.11.023](https://doi.org/10.1016/j.powtec.2020.11.023).
- [10] A. Babu, A. Templeton, A. Munshi, R. Ramesh, Nanoparticle-Based Drug Delivery for Therapy of Lung Cancer: Progress and Challenges, Journal of Nanomaterials 2013 (2013) 1–11, doi:[10.1155/2013/863951](https://doi.org/10.1155/2013/863951).

- [11] J. Liu, et al., pH-Sensitive nano-systems for drug delivery in cancer therapy, *Biotechnol. Adv.* 32 (4) (2014), doi:[10.1016/j.biotechadv.2013.11.009](https://doi.org/10.1016/j.biotechadv.2013.11.009).
- [12] J.W. Havercort, S. Kenjeres, C.R. Kleijn, Computational Simulations of Magnetic Particle Capture in Arterial Flows, *Ann. Biomed. Eng.* 37 (12) (2009), doi:[10.1007/s10439-009-9786-y](https://doi.org/10.1007/s10439-009-9786-y).
- [13] A.K. Hoshiar, T.-A. Le, P. Valdastri, J. Yoon, Swarm of magnetic nanoparticles steering in multi-bifurcation vessels under fluid flow, *J Micro-Bio Robot* 16 (2) (2020) 137–145, doi:[10.1007/s12213-020-00127-2](https://doi.org/10.1007/s12213-020-00127-2).
- [14] B. Polyak, G. Friedman, Magnetic targeting for site-specific drug delivery: applications and clinical potential, *Expert Opin Drug Deliv* 6 (1) (2009) 53–70, doi:[10.1517/17425240802662795](https://doi.org/10.1517/17425240802662795).
- [15] null Wahajuddin, S. Arora, Superparamagnetic iron oxide nanoparticles: magnetic nanoplatforms as drug carriers, *Int J Nanomedicine* 7 (2012) 3445–3471, doi:[10.2147/IJNNano.30320](https://doi.org/10.2147/IJNNano.30320).
- [16] F. Selimefendigil, H.F. Oztop, M.A. Sheremet, N. Abu-Hamdeh, Forced Convection of Fe3O4-Water Nanofluid in a Bifurcating Channel under the Effect of Variable Magnetic Field, *Energies* 12 (4) (2019), doi:[10.3390/en12040666](https://doi.org/10.3390/en12040666).
- [17] S. Dutz, Are Magnetic Multicore Nanoparticles Promising Candidates for Biomedical Applications? *IEEE Trans. Magn.* 52 (9) (2016) 1–3, doi:[10.1109/TMAG.2016.2570745](https://doi.org/10.1109/TMAG.2016.2570745).
- [18] J. Chomoucka, J. Drbohlavova, D. Huska, V. Adam, R. Kizek, J. Hubalek, Magnetic nanoparticles and targeted drug delivering, *Pharmacol. Res.* 62 (2) (2010) 144–149, doi:[10.1016/j.phrs.2010.01.014](https://doi.org/10.1016/j.phrs.2010.01.014).
- [19] M. Arruebo, R. Fernández-Pacheco, M.R. Ibarra, J. Santamaría, Magnetic nanoparticles for drug delivery, *Nano Today* 2 (3) (2007) 22–32, doi:[10.1016/S1748-032\(07\)70084-1](https://doi.org/10.1016/S1748-032(07)70084-1).
- [20] F. Hajesmaelzadeh, S. Shanehsazzadeh, C. Grüttner, F.J. Daha, M.A. Oghabian, Effect of coating thickness of iron oxide nanoparticles on their relaxivity in the MRI, *Iran J Basic Med Sci* 19 (2) (2016) 166–171.
- [21] N. Tran, T.J. Webster, Magnetic nanoparticles: biomedical applications and challenges, *J. Mater. Chem.* 20 (40) (2010) 8760–8767, doi:[10.1039/C0JM00994F](https://doi.org/10.1039/C0JM00994F).
- [22] L. Gutiérrez, et al., Synthesis Methods to Prepare Single- and Multi-core Iron Oxide Nanoparticles for Biomedical Applications, *Dalton Trans.* 44 (2014), doi:[10.1039/C4DT03013C](https://doi.org/10.1039/C4DT03013C).
- [23] M. Suciu, et al., Applications of superparamagnetic iron oxide nanoparticles in drug and therapeutic delivery, and biotechnological advancements, *Beilstein J. Nanotechnol.* 11 (2020) 1092, doi:[10.3762/bjnano.11.94](https://doi.org/10.3762/bjnano.11.94).
- [24] S. Tong, S. Hou, Z. Zheng, J. Zhou, G. Bao, Coating Optimization of Superparamagnetic Iron Oxide Nanoparticles for High T2 Relaxivity, *Nano Lett.* 10 (11) (2010) 4607–4613, doi:[10.1021/nl102623x](https://doi.org/10.1021/nl102623x).
- [25] R. Van Durme, G. Crevecoeur, L. Dupré, A. Coene, Model-based optimized steering and focusing of local magnetic particle concentrations for targeted drug delivery, *Drug Deliv.* 28 (1) (2021) 63–76, doi:[10.1080/10717544.2020.1853281](https://doi.org/10.1080/10717544.2020.1853281).
- [26] Y.-L. Liu, D. Chen, P. Shang, D.-C. Yin, A review of magnet systems for targeted drug delivery, *J. Controlled Release* 302 (2019) 90–104, doi:[10.1016/j.jconrel.2019.03.031](https://doi.org/10.1016/j.jconrel.2019.03.031).
- [27] J.H. Bernhardt, G. Brix, Safety Aspects of Magnetic Fields, in: Magnetism in Medicine, John Wiley & Sons, Ltd, 2006, pp. 76–95, doi:[10.1002/9783527610174.ch1d](https://doi.org/10.1002/9783527610174.ch1d).
- [28] M.W. Freeman, A. Arrott, J.H.L. Watson, Magnetism in Medicine, *J. Appl. Phys.* 31 (5) (1960) S404–S405, doi:[10.1063/1.1984765](https://doi.org/10.1063/1.1984765).
- [29] "Open challenges in magnetic drug targeting - Shapiro - 2015 - WIREs Nanomedicine and Nanobiotechnology - Wiley Online Library." Accessed: Nov. 15, 2020. [Online]. Available: <https://onlinelibrary.wiley.com/doi/abs/10.1002/wnnan.1311>
- [30] S. Goudarzi, M. Shekaramiz, A. Omidvar, E. Golab, A. Karimipour, A. Karimipour, Nanoparticles migration due to thermophoresis and Brownian motion and its impact on Ag-MgO/Water hybrid nanofluid natural convection, *Powder Technol.* 375 (2020), doi:[10.1016/j.powtec.2020.07.115](https://doi.org/10.1016/j.powtec.2020.07.115).
- [31] M.K.D. Manshadi, et al., Magnetic aerosol drug targeting in lung cancer therapy using permanent magnet, *Drug Deliv.* 26 (1) (2019) 120–128, doi:[10.1080/10717544.2018.1561765](https://doi.org/10.1080/10717544.2018.1561765).
- [32] F. Russo, A. Boghi, F. Gori, Numerical simulation of magnetic nano drug targeting in patient-specific lower respiratory tract, *J. Magn. Magn. Mater.* 451 (2018) 554–564, doi:[10.1016/j.jmmm.2017.11.118](https://doi.org/10.1016/j.jmmm.2017.11.118).
- [33] M. Saadat, et al., Magnetic particle targeting for diagnosis and therapy of lung cancers, *J. Controlled Release* 328 (2020) 776–791, doi:[10.1016/j.jconrel.2020.09.017](https://doi.org/10.1016/j.jconrel.2020.09.017).
- [34] M. Shamsi, A. Sedaghatkish, M. Dejam, M. Saghafian, M. Mohammadi, A. Sanati-Nezhad, Magnetically assisted intraperitoneal drug delivery for cancer chemotherapy, *Drug Deliv.* 25 (1) (2018) 846–861, doi:[10.1080/10717544.2018.1455764](https://doi.org/10.1080/10717544.2018.1455764).
- [35] M. Sefidgar, M. Soltani, K. Raahemifar, H. Bazmara, S.M.M. Nayinian, M. Bazargan, Effect of tumor shape, size, and tissue transport properties on drug delivery to solid tumors, *J. Biol. Eng.* 8 (2014) 12, doi:[10.1186/1754-1611-8-12](https://doi.org/10.1186/1754-1611-8-12).
- [36] M. Barisam, M. Shams, A three-dimensional two phase method for predicting drug delivery to tumor, *Powder Technol.* 283 (2015) 530–538, doi:[10.1016/j.powtec.2015.06.026](https://doi.org/10.1016/j.powtec.2015.06.026).
- [37] M.M. Larimi, A. Ramiar, A.A. Ranjbar, Numerical simulation of magnetic nanoparticles targeting in a bifurcation vessel, *J. Magn. Magn. Mater.* 362 (2014) 58–71, doi:[10.1016/j.jmmm.2014.03.002](https://doi.org/10.1016/j.jmmm.2014.03.002).
- [38] O. Mahian, et al., Recent advances in modeling and simulation of nanofluid flows-Part I: Fundamentals and theory, *Phys. Rep.* 790 (2019) 1–48, doi:[10.1016/j.physrep.2018.11.004](https://doi.org/10.1016/j.physrep.2018.11.004).
- [39] S. Wang, Y. Zhou, J. Tan, J. Xu, J. Yang, Y. Liu, Computational modeling of magnetic nanoparticle targeting to stent surface under high gradient field, *Comput. Mech.* 53 (3) (2014) 403–412, doi:[10.1007/s00466-013-0968-y](https://doi.org/10.1007/s00466-013-0968-y).
- [40] S. Bose, M. Banerjee, Magnetic particle capture for biomagnetic fluid flow in stenosed aortic bifurcation considering particle–fluid coupling, *J. Magn. Magn. Mater.* 385 (2015) 32–46, doi:[10.1016/j.jmmm.2015.02.060](https://doi.org/10.1016/j.jmmm.2015.02.060).
- [41] T. Lunnoo, T. Puangmali, Capture Efficiency of Biocompatible Magnetic Nanoparticles in Arterial Flow: A Computer Simulation for Magnetic Drug Targeting, *Nanoscale Res. Lett.* 10 (1) (2015), doi:[10.1186/s11671-015-1127-5](https://doi.org/10.1186/s11671-015-1127-5).
- [42] M. Momeni Larimi, A. Ramiar, A.A. Ranjbar, Magnetic nanoparticles and blood flow behavior in non-Newtonian pulsating flow within the carotid artery in drug delivery application, *Proc Inst Mech Eng H* 230 (9) (2016) 876–891, doi:[10.1177/0954411916656663](https://doi.org/10.1177/0954411916656663).
- [43] A.K. Hoshiar, T.-A. Le, F.U. Amin, M.O. Kim, J. Yoon, Studies of aggregated nanoparticles steering during magnetic-guided drug delivery in the blood vessels, *J. Magn. Magn. Mater.* 427 (2017) 181–187, doi:[10.1016/j.jmmm.2016.11.016](https://doi.org/10.1016/j.jmmm.2016.11.016).
- [44] M.K.D. Manshadi, et al., Delivery of magnetic micro/nanoparticles and magnetic-based drug/cargo into arterial flow for targeted therapy, *Drug Deliv.* 25 (1) (2018), doi:[10.1080/10717544.2018.1497106](https://doi.org/10.1080/10717544.2018.1497106).
- [45] H. Sodagar, J. Sodagar-Abardeh, A. Shakiba, H. Niazmand, Numerical study of drug delivery through the 3D modeling of aortic arch in presence of a magnetic field, *Biomech. Model. Mechanobiol.* 20 (2) (2021) 787–802, doi:[10.1007/s10237-020-01416-2](https://doi.org/10.1007/s10237-020-01416-2).
- [46] M.C. Lindemann, T. Luttko, N. Nottrodt, T. Schmitz-Rode, I. Slabu, FEM based simulation of magnetic drug targeting in a multibranched vessel model, *Comput. Methods Programs Biomed.* 210 (2021) 106354, doi:[10.1016/j.cmpb.2021.106354](https://doi.org/10.1016/j.cmpb.2021.106354).
- [47] F. Selimefendigil, H.F. Öztop, J.M. Khodadadi, Forced Convection Laminar Pulsating Flow in a 90-deg Bifurcation, *Journal of Thermal Science and Engineering Applications* 13 (3) (2020), doi:[10.1115/1.4048210](https://doi.org/10.1115/1.4048210).
- [48] International Commission on Non-Ionizing Radiation Protection, Guidelines on limits of exposure to static magnetic fields, *Health Phys.* 96 (4) (2009), doi:[10.1097/01.HP.0000343164.27920.4a](https://doi.org/10.1097/01.HP.0000343164.27920.4a).
- [49] "Carotid Bifurcation | 3D CAD Model Library | GrabCAD." <https://grabcad.com/library/carotid-bifurcation> (accessed Sep. 11, 2021).
- [50] E. Boileau, et al., A benchmark study of numerical schemes for one-dimensional arterial blood flow modelling, *International Journal for Numerical Methods in Biomedical Engineering* 31 (10) (2015) e02732, doi:[10.1002/cnm.2732](https://doi.org/10.1002/cnm.2732).
- [51] S. Siri, M. Nabaei, N. Fatouraei, Multiscale Modeling of Endothelium Derived Wall Shear Stress Regulation in Common Carotid Artery, *J. Mech.* 35 (6) (2019) 901–914, doi:[10.1017/jmech.2019.1](https://doi.org/10.1017/jmech.2019.1).
- [52] F. Selimefendigil, H.F. Öztop, A.J. Chamkha, Jet Impingement Heat Transfer of Confined Single and Double Jets with Non-Newtonian Power Law Nanofluid under the Inclined Magnetic Field Effects for a Partly Curved Heated Wall, *Sustainability* 13 (9) (2021), doi:[10.3390/su13095086](https://doi.org/10.3390/su13095086).
- [53] F. Selimefendigil, H.F. Öztop, MHD mixed convection and entropy generation of power law fluids in a cavity with a partial heater under the effect of a rotating cylinder, *Int. J. Heat Mass Transfer* 98 (2016) 40–51, doi:[10.1016/j.ijheatmasstransfer.2016.02.092](https://doi.org/10.1016/j.ijheatmasstransfer.2016.02.092).
- [54] Z. Zhang, Q. Chen, Comparison of the Eulerian and Lagrangian methods for predicting particle transport in enclosed spaces, *Atmos. Environ.* 41 (25) (2007) 5236–5248, doi:[10.1016/j.atmosenv.2006.05.086](https://doi.org/10.1016/j.atmosenv.2006.05.086).
- [55] X. Zhang, M. Luo, P. Tan, L. Zheng, C. Shu, Magnetic nanoparticle drug targeting to patient-specific atherosclerosis: effects of magnetic field intensity and configuration, *Appl. Math. Mech.-Engl. Ed.* 41 (2) (2020) 349–360, doi:[10.1007/s10483-020-2566-9](https://doi.org/10.1007/s10483-020-2566-9).
- [56] L. Kolsi, F. Selimefendigil, H. Oztop, W. Hassen, W. Aich, Impacts of double rotating cylinders on the forced convection of hybrid nanofluid in a bifurcating channel with partly porous layers, undefined (2021) Accessed: Feb. 24, 2022. [Online]. Available: <https://www.semanticscholar.org/paper/486ddc36890a3b2886d5b2ff1fb70a2ee1935f>.
- [57] F. Selimefendigil, A.J. Chamkha, Magnetohydrodynamics mixed convection in a power law nanofluid-filled triangular cavity with an opening using Tiwari and Das' nanofluid model, *J. Therm. Anal. Calorim.* 1 (135) (2018) 419–436, doi:[10.1007/s10973-018-7037-x](https://doi.org/10.1007/s10973-018-7037-x).
- [58] M. Azam, Bioconvection and nonlinear thermal extrusion in development of chemically reactive Sutterby nano-material due to gyrotactic microorganisms, *Int. Commun. Heat Mass Transfer* 130 (2022) 105820, doi:[10.1016/j.icheatmasstransfer.2021.105820](https://doi.org/10.1016/j.icheatmasstransfer.2021.105820).
- [59] J.S. Marshall, S. Li, Adhesive Particle Flow: A Discrete-Element Approach, Cambridge University Press, Cambridge, 2014, doi:[10.1017/CBO9781139424547](https://doi.org/10.1017/CBO9781139424547).
- [60] S. Savithiri, A. Pattamatta, S.K. Das, Scaling analysis for the investigation of slip mechanisms in nanofluids, *Nanoscale Res. Lett.* 6 (1) (2011) 471, doi:[10.1186/1556-276X-6-471](https://doi.org/10.1186/1556-276X-6-471).
- [61] K. E. Jansen, C. H. Whiting, and G. M. Hulbert, "A generalized-alpha method for integrating the filtered Navier-Stokes equations with a stabilized finite element method," 2000.
- [62] G. Söderlind, L. Wang, Adaptive time-stepping and computational stability, *J. Comput. Appl. Math.* 185 (2) (2006) 225–243, doi:[10.1016/j.cam.2005.03.008](https://doi.org/10.1016/j.cam.2005.03.008).
- [63] F.J. Gijsen, F.N. van de Vosse, J.D. Janssen, The influence of the non-Newtonian properties of blood on the flow in large arteries: steady flow in a carotid bifurcation model, *J. Biomech.* 32 (6) (1999) 601–608, doi:[10.1016/s0021-9290\(99\)00015-9](https://doi.org/10.1016/s0021-9290(99)00015-9).

- [64] J.M. Camacho, V. Sosa, Alternative method to calculate the magnetic field of permanent magnets with azimuthal symmetry, *Revista mexicana de fisica E* 59 (2013) 8–17.
- [65] O. Onaizah, T.L. Poepping, M. Zamir, A model of blood supply to the brain via the carotid arteries: Effects of obstructive vs. sclerotic changes, *Med. Eng. Phys.* 49 (2017) 121–130, doi:[10.1016/j.medengphy.2017.08.009](https://doi.org/10.1016/j.medengphy.2017.08.009).
- [66] D. Lopes, H. Puga, J.C. Teixeira, S.F. Teixeira, Fluid–Structure Interaction study of carotid blood flow: Comparison between viscosity models, *Eur. J. Mech. B. Fluids* 83 (2020) 226–234, doi:[10.1016/j.euromechflu.2020.05.010](https://doi.org/10.1016/j.euromechflu.2020.05.010).
- [67] D. Lopes, H. Puga, J.C. Teixeira, S.F. Teixeira, Influence of arterial mechanical properties on carotid blood flow: Comparison of CFD and FSI studies, *Int. J. Mech. Sci.* 160 (2019) 209–218, doi:[10.1016/j.ijmecsci.2019.06.029](https://doi.org/10.1016/j.ijmecsci.2019.06.029).
- [68] M. Nagargoje, R. Gupta, Effect of sinus size and position on hemodynamics during pulsatile flow in a carotid artery bifurcation, *Comput. Methods Programs Biomed.* 192 (2020) 105440, doi:[10.1016/j.cmpb.2020.105440](https://doi.org/10.1016/j.cmpb.2020.105440).
- [69] H. Gharahi, B.A. Zambrano, D.C. Zhu, J.K. DeMarco, S. Baek, Computational fluid dynamic simulation of human carotid artery bifurcation based on anatomy and volumetric blood flow rate measured with magnetic resonance imaging, *Int J Adv Eng Sci Appl Math* 8 (1) (2016) 46–60, doi:[10.1007/s12572-016-0161-6](https://doi.org/10.1007/s12572-016-0161-6).
- [70] J. Moradieghamahi, J. Sadeghiseraji, M. Jahangiri, Numerical solution of the Pulsatile, non-Newtonian and turbulent blood flow in a patient specific elastic carotid artery, *Int. J. Mech. Sci.* 150 (2019) 393–403, doi:[10.1016/j.ijmecsci.2018.10.046](https://doi.org/10.1016/j.ijmecsci.2018.10.046).
- [71] A. Iskander, et al., The Rheology of the Carotid Sinus: A Path Toward Bioinspired Intervention, *Front Bioeng Biotechnol* 9 (2021) 678048, doi:[10.3389/fbioe.2021.678048](https://doi.org/10.3389/fbioe.2021.678048).
- [72] A. Bit, et al., Three dimensional numerical analysis of hemodynamic of stenosed artery considering realistic outlet boundary conditions, *Comput. Methods Programs Biomed.* 185 (2020) 105163, doi:[10.1016/j.cmpb.2019.105163](https://doi.org/10.1016/j.cmpb.2019.105163).
- [73] X. Zhang, M. Luo, E. Wang, L. Zheng, C. Shu, Numerical simulation of magnetic nano drug targeting to atherosclerosis: Effect of plaque morphology (stenosis degree and shoulder length), *Comput. Methods Programs Biomed.* 195 (2020) 105556, doi:[10.1016/j.cmpb.2020.105556](https://doi.org/10.1016/j.cmpb.2020.105556).
- [74] M. Ahmadpour-B, A. Nooraen, M. Tafazzoli-Shadpour, H. Taghizadeh, Contribution of atherosclerotic plaque location and severity to the near-wall hemodynamics of the carotid bifurcation: an experimental study and FSI modeling, *Biomech. Model. Mechanobiol.* 20 (3) (2021) 1069–1085, doi:[10.1007/s10237-021-01431-x](https://doi.org/10.1007/s10237-021-01431-x).